ABSTRACT

Title of dissertation: MODELING AND EXPERIMENTAL MEASUREMENT OF TRIBOELECTRIC CHARGING IN DIELECTRIC GRANULAR MIXTURES

Dylan Carter
Doctor of Philosophy, 2020

Dissertation directed by: Professor Christine Hartzell
Department of Aerospace Engineering

Triboelectric charging, the phenomenon by which electrical charge is exchanged during contact between two surfaces, has been known to cause significant charge separation in granular mixtures, even between chemically identical grains. This charging is a stochastic process resulting from random collisions between grains, but creates clear charge segregation according to size in dielectric granular mixtures. Experiments in grain charging are frequently conducted with methods that may introduce additional charging mechanisms that would not be present in airless environments, and often aren't capable of measuring the precise charge of each grain. We resolved these issues through the development of a model that predicts the mean charge on grains of a particular size in an arbitrary mixture, and through experiments that do offer controlled measurement of precise grain charges. These results can be used to develop methods for electrostatic sorting to enable *in situ* resource utilization of silica-based regoliths on airless extraterrestrial bodies.

Beginning from a basic collision model for a mixture of hard spheres, we developed a robust semi-analytical model for making predictions about the charge distribution in a dielectric granular mixture. This model takes a set of assumptions about a mixture, including the continuous size distribution, collision frequencies, and charge transfered per collision, and calculates the mean charge acquired by grains of each size after all charges have been exchanged. This model allows us to explore experimental results through many different lenses. To test our predictions and provide a repeatable and flexible method for analyzing charging in a variety of granular mixtures, we designed and built our own experimental test stand. This device is housed entirely in a vacuum chamber, allowing us to induce tribocharging in dielectric grains in a controlled airless environment and measure individual charge and diameter of a grain by dropping samples through a transverse electric field.

We observed that mixtures of zirconia-silica grains containing two primary size fractions exhibited size-dependent charge segregation when charged in vacuum. Unlike in other experiments with grains charged by fluidization with a gas, we consistently observed that the small grains charged predominantly positive, while the large grains were primarily negative. We considered a variety of charge transfer mechanisms and generated predicted charge distributions for each using the modeling framework we developed. Comparing these models to the collected data, we are able to assess the viability of each potential transfer mechanism by examining properties of its resulting distribution, including the relative charge magnitudes for each size fraction, the point at which the polarity changes, and the polarity and magnitude of the charge carrier density.

The results of this work provide solid supporting evidence for the role of positive charge carriers in dielectric tribocharging. While some prior work has suggested positive ions from the atmosphere and/or adsorbed water are responsible, we have observed that even when these environmental factors are reduced or eliminated, silica-based materials still exhibit positive charge transfer. The modeling framework developed in search of a descriptive model for this effect is a useful, adaptable tool. The experimental apparatus itself, and especially in conjunction with these modeling tools, overcomes some of the more difficult challenges faced by experimentalists investigating granular tribocharging, enabling further investigation into tribocharging in regolith and other dielectric materials.

MODELING AND EXPERIMENTAL MEASUREMENT OF TRIBOELECTRIC CHARGING IN DIELECTRIC GRANULAR MIXTURES

by

Dylan Carter

Dissertation submitted to the Faculty of the Graduate School of the
University of Maryland, College Park in partial fulfillment
of the requirements for the degree of
Doctor of Philosophy
2020

Advisory Committee:
Professor Christine Hartzell, Chair/Advisor
Professor David Akin
Professor Raymond Sedwick
Professor Daniel Lathrop
Professor Derek Richardson

Acknowledgments

This research would not have been possible without the endless support of my advisor, Dr. Christine Hartzell. She kept me on track when I ran away with an idea, pushed me when I was holding back from one, and found the path when I didn't know where to go at all. I couldn't have asked for a better advisor to have my back.

I thank my committee for their guidance and expertise throughout this process: Dr. Dave Akin, Dr. Ray Sedwick, Dr. Derek Richardson, and Dr. Dan Lathrop. I also owe thanks to Dr. Elaine Oran, previously a member of my committee. Whether as my teacher or a professional reference, you have all taught me so much.

To my parents, Bill and Mena, who always knew I would end up here: thank you for giving me every advantage you could to help me reach my potential.

To my fianceé Molly Evans: there are no words that can sufficiently thank you for putting up with the long nights and longer days. I'm sure if you could leave me for a horse, you would, but here we are.

This work was supported by a NASA Space Technology Research Fellowship (NNX15AP69H). In addition to their generous financial support, I am grateful for the mentorship of my research collaborator, Dr. Carlos Calle, and his team at the Electrostatics and Surface Laboratory (ESPL) at the Kennedy Space Center SwampWorks facility. Special thanks to Jose Nuñez, Jay Philips, Paul Mackey, Mike Hogue, and Michael Johansen for their advice and experience, and for making me feel at home. And of course, I couldn't forget Jerry Wang and Joel Malissa for welcoming me as an honorary intern during my summer visits.

Back at the GRAINS lab in Maryland, I couldn't have made it through the years of research without my labmates, Thomas Leps and Dr. Anthony DeCicco. From Monday trivia to Formal Fridays, black T-shirts to three-piece suits, your friendship, not to mention design input, on this shared journey has made this all possible.

Table of Contents

List of Figures

Chapter 1: Introduction

1.1 Triboelectric Charging in Granular Media

Charge transport in dielectric granular media has long been the subject of study by the electrostatic community. The separation of charge in granular mixtures due to triboelectric charging can cause dramatic and potentially dangerous electrical discharges in both natural [1, 2, 3, 4] and man-made [5, 6, 7, 8] granular mixtures and environments. Improving our understanding of this effect is critical for both ensuring safety of persons and equipment in highly charged environments, and for utilizing this understanding to more efficiently conduct powder-handling operations like electrospraying [9] and pneumatic transport [5, 6, 7, 8, 10]. Where the granular mixture consists of only one material, such that no apparent chemical difference drives the charge exchange, it is observed that charge transfer is stochastic but follows trends according to the sizes of the grains.

The exact mechanism of charge transfer and the distribution of charge according to mixture properties remain uncertain. In part, this is due to the wide variety of possible candidates for charging mechanism and charge carrier among different materials, including trapped high-energy electrons [11, 12, 13, 14, 15], hydroxide ions or other adsorbed ions in the surface water layer [8, 16, 17, 18, 19], or broken

polymer chains [20]. Most experiments and existing models for charge exchange predict that larger grains will tend to acquire a positive charge and smaller grains will become negatively charged, on average. The degree of charge separation is influenced primarily by the size differences and mass fractions of each discrete grain size [11, 12, 13, 21, 22]. Existing models for charge exchange in granular mixtures of a single material neglect a number of important effects, especially the influence of contact area during collisions and the effect of non-discrete size distributions on charge separation, and typically underestimate the magnitude of the charge exchange [11, 21, 23]. The difficulty in obtaining detailed measurements of individual grain charge and charge distribution within the mixture, while controlling for the environmental conditions necessary to isolate a particular charging mechanism, make a consistent predictive charging model especially elusive for dielectric grains.

Triboelectric charging is also believed to occur in the dusty surface layer of airless extraterrestrial bodies like the Moon. High-energy electrons from the solar wind plasma are deposited into this insulating dusty surface material, known as regolith. This charge may be readily exchanged when the surface is agitated in future manned or robotic surface operations [24]. Not only is it important to accurately predict the magnitude and mechanism of this transfer to mitigate dangerous electrical discharge, we propose that this phenomenon may also be used as an electrostatic sieve, extracting both material components and size fractions from the regolith *in situ* for a variety of applications. Identifying an accurate tribocharging model for complex dielectric mixtures under high-vacuum conditions will be necessary to enable this application, but is difficult to accomplish using existing techniques for tribocharging

measurement.

This work improves existing tools for measuring and understanding tribocharging in granular dielectric materials. Many charge transfer mechanisms have been proposed for dielectric grains, but the nuances of how these mechanisms manifest in the distribution of charge throughout the mixture have not been fully explored. This is largely due to the difficulties inherent in measuring surface charge on micron-scale grains without influencing the charge through contact. We have created a modeling framework for predicting the mean charge distribution arising in a tribocharged mixture based on a set of assumptions about the charging process, and developed an experimental method to test these predictions. The main contributions of this work are:

- A flexible semi-analytical model for charge transfer in dielectric granular mixtures with arbitrary continuous size distributions;
- An experiment for charging dielectric granular mixtures under a controlled environment and measuring the individual charge and size distributions within the mixture in a non-invasive way;
- Evidence for the role and density of positive charge species in tribocharging in vacuum based on experiments conducted with zirconia-silica grains; and
- The foundations for a path toward understanding the relationship between certain proposed charge transfer mechanisms and their effect on the distribution and segregation of charge in a mixture.

Publications

All publications and presentations to date that resulted from this research are listed here for reference.

Journal Articles

- D. Carter and C. Hartzell, "Effect of mixture properties on size-dependent charging of same-material dielectric grains," *Physical Review E*, submitted Jan 2019.
- D. Carter and C. Hartzell, "Experimental methodology for measuring in-vacuum tribocharging," *Review of Scientific Instruments*, 90(125105), Dec 2019.
- D. Carter and C. Hartzell, "Extension of discrete tribocharging models to continuous size distributions," *Physical Review E*, 95(012901), Jan 2017.

Conference Papers

- D. Carter and C. Hartzell, "A method for measuring charge separation in granular mixtures in vacuum," *2017 Annual Meeting of the Electrostatics Society of America*, Jun 2017.
- D. Carter and C. Hartzell, "A model of granular tribocharging for dielectric mixtures with continuous size distributions," *2016 Annual Meeting of the Electrostatics Society of America*, Jun 2016

- D. Carter and C. Hartzell, "An extension of discrete tribocharging models to continuous size distributions," *Society of Satellite Professionals International (SSPI) Engineering Student Competition*, Apr 2016.

Presentations and Posters

- D. Carter and C. Hartzell, "Polarity Reversal and Charging Model for Triboelectrically Charged Silica Mixture," *2019 Annual Meeting of the Electrostatics Society of America*, Jun 2019.

- D. Carter and C. Hartzell, "Measurements of Same-Material Tribocharging in Granular Silica," *2018 AGU Fall Meeting*, Dec 2018. Poster.

- D. Carter and C. Hartzell, "Size Beneficiation of Lunar Regolith via Triboelectric Charging for In Situ Resource Utilization," *NASA Exploration Science Forum 2018*, Jun 2018. Poster.

- D. Carter and C. Hartzell, "Measurements of Granular Tribocharging by High-Speed Videography," *2018 Annual Meeting of the Electrostatics Society of America*, Jun 2018.

- D. Carter and C. Hartzell, "A model for tribocharging of regolith grains," *Dust, Atmosphere, and Plasma Environment of the Moon and Small Bodies Workshop*, Jan 2017.

- D. Carter and C. Hartzell, "An Analytical Model of Tribocharging in Regolith," *2015 AGU Fall Meeting*, Dec 2015. Poster.

Chapter 2: Literature Review

2.1 Tribocharging in Insulators

Tribocharging occurs between nearly every combination of materials, including conductors, semiconductors, and insulators. There are many different mechanisms and models for the charge exchange depending on properties of the materials. For example, in conductive materials in contact, mobile electrons in the bulk are able to easily transfer to materials with lower surface energy, allowing predictable exchange of charge that disperses evenly throughout the materials [25].

Insulators, however, exhibit far more complex charging patterns, with charge exchange attributed to many causes with various degrees of success. For contact of metals with insulators, an empirically-determined effective work function admits treatment of the charge exchange in a similar fashion to the high-conductivity case [25, 26]. However, the contact of insulators with other insulators is far less well understood. While the degree and cause of charge transfer is difficult to identify in many such cases, the direction is fairly predictable, with a particular charge polarity frequently arising after contact between certain pairs of materials.

For this reason, researchers have developed a "triboelectric series" that lists materials in order of polarity, used to predict the direction of charge transfer when

two materials from the series come into contact [27, 28]. These lists are qualitative and often unreliable due to the wide variety of possible mechanisms causing insulator charging: charge exchange has been attributed to such factors as the settling of trapped high-energy electrons [11, 12, 13, 14, 15, 21], the release of adsorbed ions [8, 19], breaking of polymer chains [20], and interactions with atmospheric ions [29], with varying degrees of accuracy.

It has also been shown that tribocharging occurs even between identical materials, despite the lack of chemical differences between the surfaces. Lowell and Truscott observed that when a dielectric material was rubbed across another identical surface, the moving surface tended to acquire a more negative charge [14, 15]. Shinbrot, Komatsu, and Zhao demonstrated that rubbing two identical insulating surfaces together in air produces an increasingly large potential difference, with the surfaces acquiring a random polarity in each experiment [29]. In general, the symmetry of same-material tribocharging causes the direction and magnitude of charge exchange to vary between experiments, suggesting that a stochastic model (e.g., high-energy electron transfer) will be more successful than previous rigidly deterministic models (e.g., the work function difference). Additionally, the transferred charge from a surface appears to be proportional to the surface area in contact, as expected for dielectric materials with low charge transport in their bulk.

Granular mixtures of a single insulating material are just as susceptible to same-material tribocharging as flat surfaces. In many cases, granular mixtures include a variety of materials, and their charge distribution is governed by these material differences; for example, pneumatic powder transport often induces significant

triboelectric exchange between powders and metal surfaces [5, 6, 7, 8]. In addition, humidity in the air and adsorbed onto grain surfaces has been shown to significantly alter charging characteristics [8, 18]. However, even granular mixtures of only a single insulating material have been shown to readily develop charge separation through same-material particle-particle collisions [13, 21, 30].

2.2 Models for Charge Transfer

When metals are involved in the charge exchange, the quantity of charge is much easier to predict than for solely insulator-to-insulator transfer. A number of studies have shown that for two conductive materials in contact, the quantity of charge transferred can be determined by the difference in surface energy of the materials [25]. Near the point of contact, electrons from the bulk of the materials rearrange themselves to equalize the energy levels of the two materials. When the materials are then separated, one material retains additional electrons acquired from the other material, which then redistribute throughout the bulk. The quantity of transferred charge can be approximated as $\Delta q_c = -\frac{C_0}{e}(\phi_1 - \phi_2)$ [25], where C_0 is the capacitance between the surfaces and ϕ is the material's work function.

Even when only one of the contacting materials is conductive, one can typically estimate the transferred charge by empirically determining the "effective work function" for that material. In 1969, Davies conducted experiments in which non-conductive polymeric materials were rubbed against a variety of metals with known work function [31]. The surface charge density was then measured, and they found

that the quantity of transferred charge was indeed linear with the metals' work functions. They were then able to determine an effective work function through which the transferred charge could be predicted when charging with other conductive materials. In 1976, Gallo and Lama would further propose a model through which a polymer's effective work function could be estimated based on the ionization energy of its monomer [26].

Still, the electron transfer model for metal-to-insulator charging has its problems, especially the lack of mobile electrons and a robust theoretical method to predict an insulator's work function. Other researchers have investigated the possibility that surface ions may be responsible for charge transfer in both metal-to-insulator as well as insulator-to-insulator charging, where the lack of mobile electrons makes it more likely that ions are responsible for charge exchange. In 1980, Lowell and Rose-Innes suggested that, when metals rub against a polymer, material from either surface can be deposited on the other surface, causing charge transfer [32]. In 2012, Burgo, *et al.* [20] measured the charge distribution on the surfaces of polymers in contact and observed patches of charge, which they attributed to the breaking of weakly bound layers and impurities in the polymer structure near the surface.

Other non-electron models for charge transfer are based on the observation that most materials in atmosphere have a thin water layer adsorbed to their surfaces. When two such surfaces come into contact, it is primarily this water layer, not the actual material in question, that is in contact. Ions dissolved here form a "double layer," with the ions near the surface being balanced by oppositely-charged ions near the surface of the double layer. Shinbrot proposed that the potential

step created between the material surface and the charged outer layer could cause charge exchange, and developed a quantitative model for this effect [33]; however, he noted that this model likely cannot fully capture the charging process on its own. Future experiments on this phenomenon, discussed in the next section, have yielded conflicting results.

Lowell and Truscott proposed a model based on their experiments into same-material tribocharging in which a number of electrons on insulator surfaces are in unfavorably high-energy states, but cannot reach low energy states due to the low conductivity of the material. During contact with another surface, these electrons are exposed to low-energy states on the other surface and can be transferred [14, 15].

Expanding upon this model, Lacks and Levandovsky proposed a mechanism for grain charging due to size differences in a mixture alone [11]. During agitation of a granular mixture, grains repeatedly collide and slide against each other, allowing all trapped electrons to achieve lower-energy states. Lacks and Levandovsky developed a model for predicting the average steady-state charge on grains of a particular size in a bidisperse mixture of a single material, demonstrating that larger grains will always acquire a positive charge in such a case.

They later expanded upon this model to include the more general case of multiple size species and the possibility for low-energy electron exchange, although they neglected the latter in simulations and analysis [12]. Particle dynamics simulations of this "population balance" model compare favorably with experimental results, with larger grains acquiring a more positive charge on average than smaller grains [11, 12, 22]. In 2009, Lacks and Kok extended the model to include a dependence of

the quantity of transferred charge on the sizes of the grains in contact [23]. In their model, electrons transfer due to tunneling during collisions, with the probability of tunneling a function of the distance between the electron on one grain and the closest point on the surface of the other grain. Assuming δ_0 is the maximum distance an electron in the ground state could tunnel, one can calculate the surface area on each grain over which electrons are able to transfer.

2.3 Experimentation

Cartwright, *et al.* [8], developed a full-scale experiment to investigate dangerous conditions that arise in pneumatic conveying of powders. In their experiments with polyethylene powders, they observed bipolar charging of the grains, such that the smallest grains charged negatively while the larger grains charged positively.

In 1994, Pence, Novotny, and Diaz [16] measured the effect of relative humidity on the charge transfer between polymer powders and steel beads. They noted that the charge magnitude increased as relative humidity rose from 0% to approximately 40%, then decreased again at higher humidities. Wiles, *et al.* [17] induced similar charging between steel spheres and a polystyrene surface, noting that the rate of charging increased linearly with relative humidity over the entire range of humidities investigated.

In 2002 and 2003, Zhao, Castle, and Inculet [30, 34] measured the distribution of charge in a variety of powders used as paint pigments in aerosols and electrostatic painting guns. They charged these grains by fluidizing a bed of these powders with

air, then dropping them through a vertical array of Faraday pail sensors. As the charged grains fell, they were accelerated by image charges toward the pails, which captured them and measured their total charge. Small grains were able to accelerate faster and therefore collected in the upper pails, while large grains collected in the lower pails. By measuring the average size and total charge of grains collected in each pail, they were able to very roughly estimate the charge distribution by size, observing again that the small grains charged negatively.

Watanabe, *et al.* [35] measured the charge transferred in a single collision between a stainless steel plate and non-conductive particles common in the pharmaceutical industry: α-lactose monohydrate, aspirin, sugar granules, and ethylcellulose granules. Grains were dropped onto the plate, with their charged measured immediately before and after the impact. The experiment was conducted in air inside a vacuum chamber, but the collision speed was varied by changing the vacuum level. Humidity and temperature were kept constant for each experiment. They observed that the transferred charge was directly proportional to the normal speed on impact, but that the equilibrium charge after repeated contacts was constant for each material.

In 2008, Shinbrot, Komatsu, and Zhao [29] investigated same-material tribocharging by rubbing together latex balloons and polycarbonate disks. The surfaces were rubbed together, then separated, measured, and neutralized by spraying with ionized air. They observed that, in each experiment, the surfaces had patches of both positive and negative charges, with one surface charging significantly more positively and the other charging more negatively. The polarity appeared to be ran-

dom in each iteration, with no correlation to prior polarities. They noted that the initial charge exchange appeared to be random, but once a dominant charge began to develop, the surface never neutralized or changed sign, only increasing in magnitude. They repeated these experiments in helium and noted that the surfaces did not significantly charge in an inert atmosphere, concluding that patches of charge recruited ions from the air to catalyze the formation of new charged patches as the surfaces moved against each other.

Forward, Lacks, and Sankaran developed a more rigorous methodology for isolating particle-particle interactions through the use of a bed fluidized with inert nitrogen [36]. In a variety of experiments, they demonstrated that the size-dependent charge polarity predicted by the high-energy electron model is independent of material and occurs in any mixture with a wide size distribution, including lunar and Martian regolith simulants [13, 37, 38]. They further showed that the degree of charge separation is highly dependent on the relative masses of each size species, as this value influences the rate at which grains collide with other species.

In 2010, Pähtz, Herrmann, and Shinbrot [1] presented a potential explanation for how non-conductive grains could charge in response to an externally-applied electric field. They proposed that the grains could become partially polarized in the direction of the field, so that collisions occurring in the direction of the electric field cause adjoining hemispheres to neutralize. They conducted an experiment using 1.6 mm glass beads in a glass container, with electrodes at the top and bottom to create a vertical electric field. Pressurized air fed in from the bottom fluidized the grains, mixing them, and they measured the number of grains lofted at various

heights. They compared this to the same quantities from a simulation based on their transfer mechanism, showing good agreement between the two.

Apodaca, *et al.* [39], conducted experiments with a range of flat polymers to determine the relationship between surface area and charge transfer in a single contact between identical polymer surfaces. They observed that the total quantity of charge transferred over repeated contacts approached asymptotic values, but that the quantity was actually proportional to the square root of the contact area, not the area itself. They concluded that properties of surface roughness and molecular-scale fluctuations in composition play a signficant role in charge transfer, possibly more so than the contact area.

In 2012, Sow, *et al.* [40] observed that certain conditions could cause the direction of charge transfer between identical materials to reverse. Using balloons made from latex rubber and inflated to varying degrees, they noted that by varying the surface strain through inflation and deflation, they could control the charge polarity on each surface. These experiments were conducted in an environment purged with nitrogen.

In pursuit of a method for electrostatic beneficiation of regolith, Trigwell, *et al.* [41, 42, 43] conducted experiments at Kennedy Space Center to assess the feasibility of separating particular chemical components of regolith by allowing them to tribocharge against a static charger. Materials tested for this charger were aluminum, copper, and polytetrafluoroethylene. They demonstrated that such a device could indeed be capable of enriching a regolith sample to higher concentrations of a desired component (ilmenite, in their case).

Jaeger and Waitukaitis, *et al*, developed a more sophisticated method for measuring the actual charge on each grain to further investigate the predictions of Lacks and Levandovsky's model [21, 44]. Their results also agreed with the polarity predicted by the original model, but they observed that the magnitude of the charge was too large to be simply caused by trapped electrons. They suggested that alternative mechanisms such as ion transfer or interactions with the atmosphere may play a role in charging.

2.4 Summary

Throughout the last few decades, many researchers have attempted to identify a consistent model for insulator tribocharging. The results of their experiments vary dramatically, agreeing consistently on some results, such as the role of surface roughness on the charging process. However, frequently their results appear to be in conflict; some show that charge exchange is proportional to contact area, other times to its square root. Some experiments suggest that charging continues up to the Paschen limit with repeated contact, only ceasing when electrical discharge occurs; others identify an apparent asymptote or even eventual reversal of polarity. The issues with same-material tribocharging are even greater due to the lack of a clear driving factor like surface energy. In the case of granular materials, the difficulty in measuring individual grain charge to obtain a consistent charge profile makes progress slow. In this thesis, we develop techniques that may provide a solution to many of these challenges.

Chapter 3: Modeling Charge Transfer in Continuous Mixtures

This chapter contains material published in D. Carter and C. Hartzell, "Extension of discrete tribocharging models to continuous size distributions," *Physical Review E*, 95(012901), Jan 2017 [45].

In this chapter, we expand existing models of tribocharging to make predictions about the charge distribution in mixtures with a continuous size distribution. To date, analytical models for charge exchange typically apply only to very simple mixtures of grains in which each grain is assumed spherical and has one of two allowed sizes [1, 11, 12, 13, 21, 23]. Many of these models describe charge exchange events as identical for all pairs of grains regardless of grain size, despite the fact that the final charge is observed to be size-dependent [11, 12, 13, 21, 22].

In their initial discussion, Lacks and Levandovsky note that they have ignored a variety of phenomena, including the effect of aspherical shapes, sliding contact, and electrostatic forces between grains, which may alter the charge exchange rate [11]; Kok and Lacks similarly leave out these factors [23]. We have modified these models by including a new method for calculating contact area differences between grains, which drive the amount of charge exchanged during a collision. When two real objects collide, they deform slightly such that they develop an approximately

flat contact area between them, across which trapped electrons are able to move. By assuming each collision exchanges a size-independent number of electrons from each grain, Lacks and Levandovsky neglect the effect of grain size differences and assume electron transfer rate is independent of collision area. This area is determined by the size and collision energy of the grains, and therefore increases with increasing grain size. Experiments on sphere-to-surface contact charging have demonstrated that the exchanged charge is indeed proportional to contact area, and that contact area can be varied through changes in collision speed and sphere size [35, 46, 47]. While the contact area formulation in Kok and Lacks' work also suggests a proportional relationship between collision area and transferred charge, it requires that grains are treated as hard spheres, so that changes in collision energy have no effect on the charge [23].

Because the magnitude of insulator tribocharging is shown to be highly dependent on the area in contact [14, 15, 22, 29, 46], we introduce an additional term A_{ij}, the contact area between grains of radii R_i and R_j during a collision. This causes the amount of transferred charge during a collision to depend upon the relative sizes of the grains in contact, changing the properties of the charge distribution and making new predictions about charging trends for various size distributions. While we initially assume that the carrier species consists of electrons, this model provides a generic, flexible framework for describing how a particular charge transfer mechanism manifests as a charge distribution function. From this standpoint we will determine which transfer models most accurately represent real granular mixtures and assess the implications for our understanding of granular tribocharging as a

whole.

3.1 Model Assumptions

For the purposes of deriving this model, we will adopt the charge transfer mechanism proposed by Lowell and Truscott [14, 15] and further elaborated by Lacks and Levandovsky [11, 12]. Each grain is assumed to be a solid sphere of radius R; its surface area is therefore $4\pi R^2$. The surface area density of trapped high-energy electrons is σ_H and is initially the same for all grains. Its value at time $t = 0$ (before charge exchange due to mixing) is given by σ_0, at which time all grains are electrically neutral. According to the trapped electron model, each collision exposes some number of high-energy electrons that each have a random probability of being transferred; we will denote this probability as f_H. In addition, we will assume that each collision involves some characteristic contact area A_{ij}, where the colliding grains have radii R_i and R_j. We will further assume that the relative speed between grains is size-independent and equal for all grains, and they are all composed of the same material; therefore, the contact area is a function of the grains' radii only. This allows us to express the number of high-energy electrons transferred from a grain of radius R_i to a grain of radius R_j as $f_H \sigma_{H,i} A_{ij}$. Note that the average surface density of electrons $\sigma_{H,i}$ is a function of time, and therefore varies throughout the mixing process.

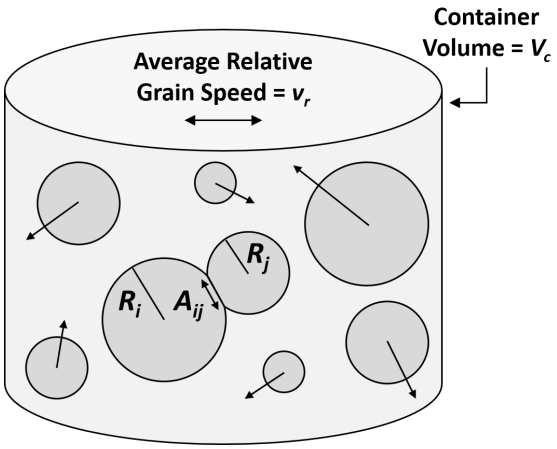

Figure 3.1: Diagram of physical system considered. Grains with a normalized size distribution given by $g(R)$ are mixed in a container of volume V_c. Mixing is performed by moving the container with average speed v_r, such that the grains inside also move with average speed v_r. The grains are then assumed to move in random directions with average speed v_r as well. When a grain of radius R_i collides with a grain of radius R_j, some contact area is formed in region A_{ij}. High-energy electrons in this region are capable of transferring between the two grains and settling into stable low-energy states.

3.1.1 Collisions

In order to estimate the collision rates between grains, we assume that all grains move at approximately the same speed, and therefore that the average relative speed between two grains is a constant, here called v_r. For very small particles, their kinetic energy is frequently governed by thermal effects and the electromagnetic force, resulting in size- and/or charge- dependencies for the particle speed. However, we will assume for this model that the motion of the grains is dominated by some other external force that gives each grain an average speed of v_r relative to the other grains in the bulk, e.g. a uniform acceleration applied to a bed of loose grains. See Figure 3.1 for an illustration of this collision process.

We can use the relative speed between grains to estimate the collision rates

as grains move through the mixure. Consider a single grain of radius R_i moving against a background of grains of radius R_j. The first grain moves with speed v_r relative to the background grains. In some time Δt, the grain moves a distance $v_r \Delta t$. In this time, it collides with any grains whose centers are a distance $R_i + R_j$ from the axis of its motion. Therefore, the moving grain collides with any grains within the volume $\pi (R_i + R_j)^2 v_r \Delta t$. If our control volume is V_c and there are n_j grains with radius R_j in the mixture, then the rate at which our grain of radius R_i collides with grains of radius R_j is ω_{ij}, where:

$$\omega_{ij} = \frac{\pi v_r n_j}{V_c} (R_i + R_j)^2 \tag{3.1}$$

3.1.2 Size Distribution

Previous tribocharging models have been developed specifically for application to size distributions consisting of two discrete sizes [11, 13]. These models are restrictive, as unsieved granular mixtures in nature are more accurately represented by continuous size distribution functions. While bidisperse mixtures are much easier to manipulate analytically and are relevant to simple tribocharging experiments, they cannot explain or predict phenomena in natural granular mixtures. Thus, we will consider charge exchange in an arbitrary continuous grain size distribution.

Consider a mixture of grains with a probability distribution of radii given by $g(R)$; that is, the fraction of grains in the mixture with a radius within dR of R is $g(R)dR$. The distribution is normalized such that $\int_0^\infty g(R)dR = 1$. As a result, the

number of grains within dR_j of radius R_j (defined as n_j) is equal to $n_0 g(R_j) dR_j$, where n_0 is the total number of grains in the mixture. To find the value of n_0, we define the total mass of the mixture as M_0; we use this parameter because of the ease with which this is directly measured in experiments. Using this definition, and defining the mass density of grains as ρ_M, we can determine n_0 by integrating the mass of all grains in the mixture as follows:

$$M_0 = \frac{4}{3}\pi \rho_M n_0 \int_0^\infty R^3 g(R) dR \tag{3.2}$$

The use of a continuous size distribution also has important implications for the collision rate. Recall that the collision rate ω_{ij} depends upon the number of grains n_j of radius R_j in the mixture. When we expand this term, we get a differential term dR_j in the definition of ω_{ij}. This will be important when we calculate the rate at which high-energy electrons are transferred to the mixture background.

3.1.3 Electron Transfer Rates

We begin by considering the rate at which a single grain of radius R_i loses electrons to low-energy states on grains of radius R_j during mixing. We have previously derived an expression for the frequency of such collisions ω_{ij}, as well as an expression for the number of electrons transferred per collision at a given time t. Suppose that the charge and number of acquired electrons on a grain does not affect the rate at which it continues to donate or acquire electrons during collisions. We can then write an expression for the rate at which high-energy electrons on a grain

of radius R_i are lost:

$$\frac{d}{dt}\left(\sigma_{H,i}\right)|_{R_j} = -\frac{\omega_{ij} f_H \sigma_{H,i} A_{ij}}{4\pi R_i^2} \tag{3.3}$$

This expression gives only the rate at which electrons are lost to grains in a narrow band of radii around R_j. To obtain the rate at which the grain loses electrons to all other grains in the mixture background, we integrate this expression over the range of all grain sizes R_j:

$$\frac{d\sigma_{H,i}}{dt} = -\alpha_i \sigma_{H,i} \tag{3.4}$$

$$\alpha_i = \frac{v_r n_0 f_H}{4R_i^2 V_c} \int_0^\infty A_{ij} \left(R_i + R_j\right)^2 g(R_j) dR_j \tag{3.5}$$

For the time being, since we have not defined an expression for A_{ij}, we cannot evaluate this integral. We shall find that for most size distributions, it will be necessary to evaluate this integral numerically.

3.1.3.1 Electron Loss Fraction

In the previous section, we defined the average rate at which a single grain of radius R_i, representating the average grain of that radius, loses high-energy electrons to grains of radius R_j. As we saw, this rate is given as a continuous function (averaged over the discrete collision events that happen over much smaller time scales) and is directly proportional to the mobile electron density $\sigma_{H,i}(t)$. Suppose

that we wished to find the fraction of all electrons currently being transferred from a grain of radius R_i that were going to grains of a specific size R_j. This quantity is critical to understanding the nature of size-dependent charge separation. We note that this quantity, here called f_{ij}, can be equivalently described as the ratio between the rate of electron transfer to size species R_j, given by Equation (3.3), and the rate of overall electron transfer to grains of all sizes, given by Equation (3.4):

$$f_{ij} = \frac{A_{ij} \left(R_i + R_j\right)^2 g(R_j) dR_j}{\int_0^\infty A_{ik} \left(R_i + R_k\right)^2 g(R_k) dR_k} \tag{3.6}$$

We have replaced the variable of integration R_j in the denominator with the dummy variable R_k, to distinguish it from the actual variable R_j in the numerator, the size of the grain band with which our single grain is colliding. Note that the electron density cancels out, and the fraction of electrons transferred is a constant fraction with a dependence on grain radii and the size distribution only. Importantly, we note that we can now express the rate of change of the high-energy electron population in the following simple ways:

$$\frac{d\sigma_{H,i}}{dt}|_{R_j} = f_{ij} \frac{d\sigma_{H,i}}{dt} = -\alpha_i f_{ij} \sigma_{H,i} \tag{3.7}$$

3.1.3.2 Collision Area

Now that we have identified all the required relationships to make predictions about the average final charge, we turn our attention to the collision area. For the analysis up to this point, we have assumed that each grain is a hard sphere of a

particular radius R. The contact area between two perfectly spherical hard grains is simply a point, but such a model neither contributes to our understanding of granular tribocharging nor fits experimental data regarding tribocharging in general. In experiments on rubbing flat surfaces together, the exchanged charge is directly proportional to the area exposed to contact, and collisions between small grains slide against each other rather than simply rebound at a point contact [35, 46, 47]. From this observation, we may conclude that the exchange of charge in real collisions between grains will be heavily dependent on the size of the grains. Specifically, because electron transfer in other systems tends to depend on the surface area, we expect to see a similar area dependence in sliding grain collisions.

The inclusion of a collision area term is a significant improvement over the typical approach used in many granular tribocharging models, and allows us to explore a variety of possible transfer mechanisms. The model developed by Lacks and Levandovsky, and frequently employed to make predictions in various tribocharging experiments, assumes that a constant number of electrons (frequently one) is transferred during each collision. This is analogous to the assertion that $1 = f_H A_{ij} \sigma_{H,i}(t)$, using the framework developed for our model. While this appears to create problems due to the fact that $\sigma_{H,i}$ loses its dependence on time, we note that in the loss fraction f_{ij} (which we will later see is the most important term in predicting the final charge), the electron density divides out. Therefore, in calculating the final charge on the grains, the result is identical to the assumption that A_{ij} is a constant and also divides out. Other models have also been developed to include a contact area term, especially that of Kok and Lacks [23]; however, we believe that

our implementation better represents what is known about the relationship between collision speed and transferred charge. In using a "maximum tunneling distance" as the effective boundary of the contact area, Kok and Lacks have developed a framework in which the effective contact area is different for the two grains, due to the difference in surface curvature [23]. In our model, the contact area is the same for the two grains, which agrees with previous experiments and models exploring the effect of collision energy on contact area and transferred charge [14, 15, 29, 46].

In Gugan's treatment of Hertz's theory for collisions between two spheres [48], the collision area is given in terms of the collision speed U, reduced radius $R_* = \frac{R_i R_j}{R_i + R_j}$, reduced mass $M_* = \frac{m_i m_j}{m_i + m_j} = \frac{4\pi\rho_M R_i^3 R_j^3}{3\left(R_i^3 + R_j^3\right)}$, and effective elastic coefficient $X_* = \frac{1-\nu_i^2}{E_i} + \frac{1-\nu_j^2}{E_j} = \text{constant}$. Because we are here assuming that all grains are of the same material, they all have the same density, modulus E, and Poisson's ratio ν. We have also assumed that the relative speed between any two grains is v_r, so all factors involving only these terms can be dropped for simplicity:

$$A_{ij}^{2.5} = 16.4 v_r^2 M_* R_*^2 X_* \propto M_* R_*^2 \tag{3.8}$$

Now we expand these quantities and solve for A_{ij}:

$$A_{ij} \propto r_{ij} R_i R_j \tag{3.9}$$

$$r_{ij} = \frac{R_i R_j}{\left(R_i^3 + R_j^3\right)^{0.4} \left(R_i + R_j\right)^{0.8}} \tag{3.10}$$

Because we are considering an area term, we have rearranged the expression so that it can be written as the product of the radii of the involved grains and a non-dimensional term r_{ij}. Note that this looks very similar to the square of the reduced radius defined above. This makes logical sense, as real collisions are not simply point contacts and will involve an amount of contact area highly dependent on the size and shape of the grains.

3.2 Steady-State Solutions to the Charge Distribution Function

3.2.1 Solutions for Continuous Size Distributions

To predict the grain charge at some time t after the initiation of mixing, we must first calculate the rate at which a single grain accumulates low-energy electrons. Consider now that each grain of radius R_j gives a fraction f_{ji} of its high-energy electrons to grains of radius R_i. The rate at which electrons are given in this way after some time t is $-4\pi R_j^2 n_j f_{ji} \frac{d\sigma_{H,j}}{dt}$. Therefore, if we divide this quantity by n_i, the number of grains of radius R_i, we get the rate at which low-energy electrons settle on the average grain of size R_i. Using Equation (3.4), the change in charge $Q_{L,ij}(t)$ contributed by these low-energy electrons from grains of radius R_j is:

$$\frac{dQ_{L,ij}}{dt} = -4e\pi\alpha_j R_j^2 f_{ji} \frac{n_j}{n_i} \sigma_{H,j} \tag{3.11}$$

To obtain the overall contribution to the charge from all other grain sizes, we simply integrate this expression over all sizes R_j. Meanwhile, the grain is also

losing high-energy electrons due to each of these collisions. The rate at which it loses electrons can be given as the rate of change of surface electron density (found in Equation (3.4)) multiplied by the surface area and electron charge $-e$:

$$\frac{dQ_{H,i}}{dt} = -4e\pi R_i^2 \frac{d\sigma_{H,i}}{dt} = 4e\pi\alpha_i R_i^2 \sigma_{H,i} \tag{3.12}$$

The overall rate of change of the charge of a single grain of radius R_i will be given by the sum of these rates:

$$\frac{dQ_i}{dt} = \frac{dQ_{H,i}}{dt} + \int_{dR_j} \frac{dQ_{L,ij}}{dt} \tag{3.13}$$

Recall from Equation (3.4) that the surface electron density can be written as an exponential decay function, with $\sigma_{H,i}(t) = \sigma_0 e^{-\alpha_i t}$. We can make this substitution and integrate over time to obtain an expression for the actual charge at time t:

$$Q_i(t) = 4e\pi\sigma_0 \left[R_i^2 \left(1 - e^{-\alpha_i t}\right) - \int_0^\infty R_j^2 f_{ji} \frac{n_j}{n_i} \left(1 - e^{-\alpha_j t}\right) \right] \tag{3.14}$$

The above expression accounts for the fact that, at time $t = 0$, the grains are electrically neutral. By taking the time to infinity, we get an expression for the charge once all high-energy electrons have settled into low-energy states. This causes the exponential terms to die out, leaving only the following expression:

$$Q_{i,final} = 4e\pi\sigma_0 \left(R_i^2 - \int_0^\infty \frac{R_j^2 A_{ij} \left(R_i + R_j\right)^2 g(R_j) dR_j}{\int_0^\infty A_{jk} \left(R_j + R_k\right)^2 g(R_k) dR_k} \right) \tag{3.15}$$

Equation (3.15) is an expression for the final charge on a grain of arbitrary

size R_i in a mixture of grains with size distribution $g(R)$ after all mobile charges have settled into their preferred states. From the definition of the contact area, we can see that these integrals do not have an obvious closed-form solution (although the complexity is significantly reduced by applying Lacks and Levandovsky's equal contact area assumption). In addition, the use of an arbitrary size distribution function also prevents us from directly solving the integral in the general case. Therefore, solutions to the final charge equation must be obtained through numerical integration. This will be especially useful in the case of unusual size distribution functions, such as Taylor series curve fits to granular mixtures found in nature, where analytical solutions introduce unnecessary complexity.

3.2.2 Solutions for Discrete Size Distributions

Although a continuous size distribution is a better approximation of a real granular mixture than a set of discrete sizes, it is still instructive to explore how this model behaves in the case of a discrete size distribution, in order to allow comparison to both Lacks and Levandovsky's original model and to experimental observations. As discussed previously, most existing models to predict charging in laboratory mixtures employ a discrete size distribution, typically of only two primary grain radii, which we will here call R_1 and R_2, where R_1 is the larger size. This size distribution can be represented by a sum of two Dirac delta functions, which can be thought of as infinitely narrow normal distributions such that only two grain sizes are represented. Therefore, our size distribution will look like:

$$g(R) = \frac{k_1\delta_1 + k_2\delta_2}{k_1 + k_2}, \quad \delta_i = \delta\left(R - R_i\right) \tag{3.16}$$

The weights k_1 and k_2 are related to the mass of each size species. The mass of a single species i is given by the following expression:

$$M_i = \frac{4\pi\rho_M n_0 k_i R_i^3}{3\left(k_1 + k_2\right)} \tag{3.17}$$

We can define a set of non-dimensional constants $d = \frac{R_2}{R_1} < 1$ and $m = \frac{M_2}{M_1} > 0$. We will find that this greatly simplifies our analysis. Plugging the mass relationships and non-dimensional constants into our expression for the size distribution, we obtain the following:

$$g(R) = \frac{d^3\delta_1 + m\delta_2}{d^3 + m} \tag{3.18}$$

Since we have already obtained an expression for the final charge, we need only plug this size distribution into Equation (3.15) and solve. Consider first the charge on grains of radius R_1, the larger size species. The grain charge expression contains two nested integrals. The integral in the denominator of Equation (3.15), here represented by I_0, is:

$$I_0(R_j) = \int_0^\infty A_{jk}\left(R_j + R_k\right)^2 g(R_k) dR_k \tag{3.19}$$

Note that this expression is independent of R_i, the grain species size that we are investigating (which here is R_1). Now consider the remaining integral:

$$I(R_i) = \int_0^\infty \frac{R_j^2 A_{ij} \left(R_i + R_j\right)^2 g(R_j)}{I_0(R_j)} dR_j \tag{3.20}$$

For the case of discrete sizes, we can analytically solve this integral using the definition of an integral of Dirac delta functions δ_k over a domain containing R_k and plug this into the expression in Equation (3.15) for charge on grains of size R_i:

$$Q_{i,final} = e\pi\sigma_0 \left(4R_i^2 - \frac{d^3 A_{i1} \left(R_i + R_1\right)^2}{d^3 A_{11} + msA_{12}} - \frac{mA_{i2} \left(R_i + R_2\right)^2}{dsA_{21} + mA_{22}}\right) \tag{3.21}$$

Before substituting for R_i, we can first expand A_{ij} in terms of the grain sizes R_i and R_j. Recall that this term is symmetric in i and j; that is, $R_{ij} = R_{ji}$. Therefore, we can be certain that $R_{12} = R_{21}$. Furthermore, we can simplify the algebra by defining $r = r_{12}$ and $s = \frac{1}{4}\left(1 + d\right)^2 < 1$, which are terms that appear frequently in the reduced expression. The expression reduces significantly in the case where $i = j$:

$$r_{ii} = \frac{2^{1.2} R_i^2}{\left(2R_i^3\right)^{0.4} \left(2R_i\right)^{0.8}} = 1, \quad A_{ii} = R_i^2 \tag{3.22}$$

$$r = d\left(\frac{2}{s\left(1 + d^3\right)}\right)^{0.4}, \quad A_{12} = rR_1R_2 \tag{3.23}$$

Finally, we can substitute the grain radii R_1 and R_2 for R_i in Equation (3.21) to find the net charge on grains of each species:

$$Q_{1,final} = 4e\pi\sigma_0 \frac{R_1^2 msr\,(m-d)\,(d-sr)}{(d^2+msr)\,(dsr+md)} \tag{3.24}$$

$$Q_{2,final} = -4e\pi\sigma_0 \frac{R_1^2 d^3 sr\,(m-d)\,(d-sr)}{(d^2+msr)\,(dsr+md)} \tag{3.25}$$

3.3 Analysis

We can demonstrate that these charge equations obey the law of charge conservation; that is, the total charge on grains of size R_1 is equal and opposite to the total charge on grains of size R_2, as we have assumed that all grains start out electrically neutral. The net total charge is $Q_0 = n_1 Q_1 + n_2 Q_2$, where $n_i = \frac{3M_i}{4\pi\rho_M R_i^3}$ is the number of grains in the mixture with radius R_i. Performing this calculation, we get the following conservation condition:

$$Q_0 = \frac{3M_1}{4\pi\rho_M R_2^3}\left(d^3 Q_1 + mQ_2\right) = 0 \tag{3.26}$$

From Equations (3.24) and (3.25), we can see that $d^3 Q_1 = -mQ_2$. The cancellation of terms resulting in net charge neutrality supports the validity of the assumptions leading to this model; although real mixtures will have a wide spread in charge within grain sizes, our average charge simplification has clearly not resulted in a violation of charge conservation. In the following sections, we will explore additional differences between our new charge distribution function and the model proposed by Lacks and Levandovsky.

3.3.1 Comparison of Continuous and Discrete Models

The original models for granular tribocharging considered only a finite number of discrete grain radii. However, a far more realistic distribution when the mixture is composed primarily of specific sizes is a sum of normal distributions. While even this may not be sufficient to properly model the size distribution found in most naturally-occuring granular mixtures, it is an instructive example in the differences and similarities between our continuous model and the discrete model. We will consider a grain mixture composed of a sum of normal distributions centered around two primary sizes R_1 and R_2, given below:

$$g(R) = k_1 e^{-a_1(R-R_1)^2} + k_2 e^{-a_2(R-R_2)^2} \tag{3.27}$$

Note that, although it is best practice to normalize this distribution function to $\int_0^\infty g(R)dR = 1$, the fact that the distribution only ever appears in both the numerator and denominator of a ratio suggests that the distribution need only be normalizable, but not actual normalized, as the normalization factor will divide out. We will also specify that $R_2 < R_1$ and define $k = \frac{k_2}{k_1}$ for the sake of convenience and consistency. Here k_i is a factor determining the height of the Gaussian peak corresponding to the distribution of grains of size R_i, so that k is the height of the R_2 peak relative to that of R_1. The coefficients a_1 and a_2 in the exponents are related to the standard deviation of the distributions, a measure of the width of the peaks. Each of these properties can be calculated from the experimentally measured

size distribution of a sample of the mixture.

Consider now the case for which $R_1 = 100\mu\text{m}$, $R_2 = 50\mu\text{m}$, $a_1 = a_2 = 0.005\mu\text{m}^{-2}$, and $k = 8$. The size distribution is shown in Figure 3.2a for a non-dimensional form of Q_{final}, where:

$$Q^* = \frac{Q_{final}}{4e\pi\sigma_0 R_1^2} \tag{3.28}$$

We can calculate the charge distribution for two cases: the constant contact area assumption made by Lacks and Levandovsky's model, and the size-dependent contact area model using the definition for A_{ij} described above. The final charge distribution is given in Figure 3.2b. Note that the constant contact area assumption produces a parabolic charge distribution, in which smaller grain sizes acquire an average negative charge while larger grains become more positively charged. On the other hand, the charge distribution for the size-dependent contact area model appears more closely related to a cubic function, with an additional peak near the small end of the grain size distribution. This means that the smallest grains actually acquire a positive charge, while many large grains are also negatively charged.

3.3.2 Polarity Reversal

The apparent reversed charge polarity in the case of size-dependent collision area goes against conventional predictions for granular insulator tribocharging. Lacks and Levandovsky's model predicts that mixture properties have no effect on the polarity, and experiments to date seem to support this assertion [11, 12, 13, 21].

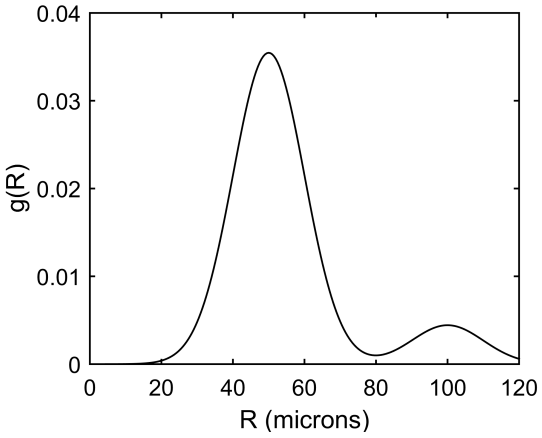

(a) Normalized particle size distribution function $g(R)$ in the form of Equation (3.27), with $k_2/k_1 = 8$, $a_1 = a_2 = 0.005\mu\text{m}^{-2}$, $R_1 = 100\mu$m, and $R_2 = 50\mu$m.

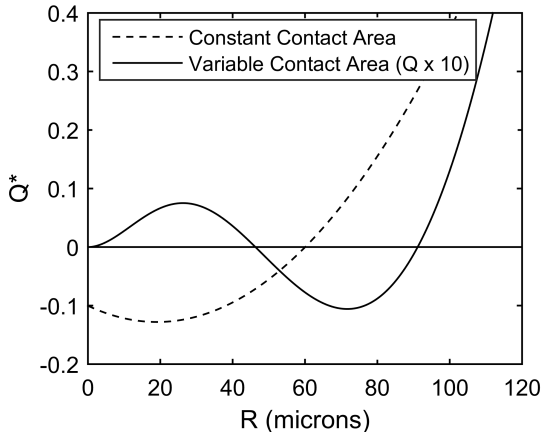

(b) Non-dimensional charge distribution function corresponding to size distribution in (a) (solid line, magnified x10 for clarity). For comparison, the distribution using $A_{ij} = \text{constant}$ is overlayed (dashed line).

Figure 3.2: Non-dimensional charge distribution $Q^* = Q(R)/4e\pi\sigma_0 R_1^2$ for a specified size distribution function.

In the following sections, we dissect the final charge expression given in Equation (3.15) to explore the parameters that determine charge polarity. We find that the definition of the area term A_{ij}, as well as the mixture parameters d and m, play a significant role in determining the final charge polarity in a bidisperse (or nearly bidisperse) mixture.

3.3.2.1 Bidisperse Mixtures

Recall that each of the non-dimensional terms m, d, r, and s is positive for all sizes R_1 and R_2. Therefore, in Equations (3.24) and (3.25), while the denominator is necessarily always positive, the negative terms in the numerator make the sign ambiguous at first glance. In previous models, the larger grain size in a bidisperse mixture always acquires a positive charge, a prediction supported by experimental

data; however, these models did not include an area term A_{ij}. For our model, we will explore the sign of the numerator of the fraction in Equation (3.24):

$$sgn(Q_{1,final}) = sgn\left[(m-d)\left(d-sr\right)\right] \tag{3.29}$$

We can expand the expression $d - sr$ in terms of only d as follows:

$$d - sr = d\left(1 - \left[\frac{(1+d)^3}{4\left(1+d^3\right)}\right]^{0.4}\right) > 0 \tag{3.30}$$

It can be trivially shown that the bracketed expression ranges between 1/4 (as d approaches 0) and 1 (as d approaches 1); we can be sure then that $d - sr$ is positive for all values of d. Therefore, the sign of the charge on grains of size R_1 is entirely determined by the simple expression $m - d$, the difference between the ratio of masses of the two species and the ratio of their radii. Specifically, the larger grains will only achieve the traditionally-predicted positive polarity if the ratio of their mass to the mass of the smaller grains is larger than the ratio of their radius to the radius of the smaller grains. Unfortunately, experiments up to this point could neither confirm or refute this prediction. This may be due to a general lack of reporting of mass ratios in granular tribocharging experiments, as this value affects only the relative magnitude of average grain charge in the models used and is of significantly less interest than the size ratio d. In the following section, we will find that this polarity reversal also appears in the continuous distribution model, but the exact conditions required to elicit this behavior are more difficult to describe in closed form.

We have already shown (in Section 3.1.3.2) that Lacks and Levandovsky's simplification of a single electron transfer per collision is functionally equivalent to the assumption that all contact areas are equivalent. To better understand the influence of the area term on the charge polarity, we can once again calculate the charge on a grain of size R_1, with the area term left as a variable. We are particularly interested in the ratio of contact areas, so let us define an additional non-dimensional term $a_{ij} = \frac{A_{ij}}{A_{11}}$. From Equations (3.21) and (3.28):

$$Q_1^* = msa_{12}\left(\frac{ma_{22} - d^3 - sa_{12}(m-d)}{(d^3 + ma_{12}s)(da_{12}s + ma_{22})}\right) \tag{3.31}$$

Although we have not yet defined A_{ij} in this example, we will make the very basic assumption that, due to the geometry of the grains, collisions between two larger grains cannot (on average) have smaller contact areas than collisions between two smaller grains. Thus we will state only that $a_{22} \leq a_{12} \leq 1$. If the contact areas are equal, then $a_{22} = a_{12} = 1$ and we obtain the expression found by Lacks and Levandovsky:

$$Q_1^* = ms(1-d)\frac{d(1+3d) + m(3+d)}{4(d^3+ms)(ds+m)} > 0 \tag{3.32}$$

Because $d < 1$ by definition, we see that Equation (3.32) must always be positive when the contact area term is neglected. When the contact area is not neglected, we can determine what properties A_{ij} must have in order to result in a polarity reversal. Consider now the sign of Equation (3.31):

$$sgn\left(Q_1^*\right) = sgn\left[d\left(s - \frac{d^2}{a_{12}}\right) + m\left(\frac{a_{22}}{a_{12}} - s\right)\right] \tag{3.33}$$

Now, both $\frac{a_{22}}{a_{12}}$ and s have values less than 1, and $s > d^2$ for all $d < 1$. Therefore, if $a_{12} < 1$ for $d < 1$ and approaches 1 more slowly than $\frac{d^2}{s}$, then the first term will be negative for all values of d greater than some critical value. Furthermore, the second term will be negative above a different critical value for d if a_{22} approaches 1 more slowly than sa_{12}. The relationship between these rates, and the value of m in the mixture, will determine the final value of d for which the entire quantity Q_1 is negative. Because we are dealing with areas here, we expect that a_{22} will have a d^2 dependence and a_{12} will have approximately a d dependence (if any at all). Since a_{12} is approximately of order d^1, we do in fact expect that the first parenthetical expression goes as $s-d$ while the second goes as $d-s$, suggesting that Q_1 is proportional to $m - d$. This reaffirms our observation of the polarity reversal derived above in Equation (3.29).

3.3.2.2 Continuous Mixtures

It is important to note that, because we are working with a continuous distribution, the concept of polarity in the sense used in the discrete model is ambiguous. For example, it can be shown that for a size distribution composed of two normal distributions like the one used Figure 3.2a, the resulting charge distribution always takes on the approximately-cubic form seen in Figure 3.2b. However, the contribution to the charge from each Gaussian peak varies in a way that reflects the polarity

reversal seen in the discrete case. This manifests through a shift in the zeroes of the continuous charge distribution; for example, as the parameters of the size distribution approach the conditions required for a polarity reversal, the negative region of the charge distribution shifts toward the larger grain sizes. This causes larger grains to become more negatively charged, while smaller grains become more positively charged overall. Figure 3.3 demonstrates the effect of this phenomenon as the size peaks vary in width. This illustrates the importance of using a continuous grain size distribution rather than a simple discrete size model: the charge distribution is highly dependent on many parameters ignored by the discrete model, especially the width of the peaks in the distribution.

We have also seen how the charge polarity depends primarily on m and d in a primarily two-species distribution when the area term is included. We can plot the non-dimensional charge Q_1^* on grains of radius R_1 against the mixture parameters k and d to better understand their effect. Recal that we can write $m-d$ as $d\,(kd^2-1)$. Therefore, the polarity reverses (Q_1^* becomes negative) with decreasing k and d. In Figure 3.4, we see this trend: the critical value of R_2 below which Q_1^* is negative occurs at larger values for decreasing k.

3.3.2.3 Compared to Previous Experiments

The charge transfer model proposed here predicts that, for certain grain size distributions, larger grains charge negatively and smaller grains charge positively. This phenomenon has not been reported in experiments to date, but the lack of

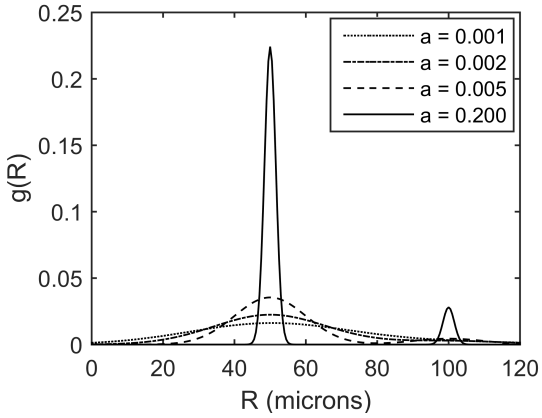

(a)

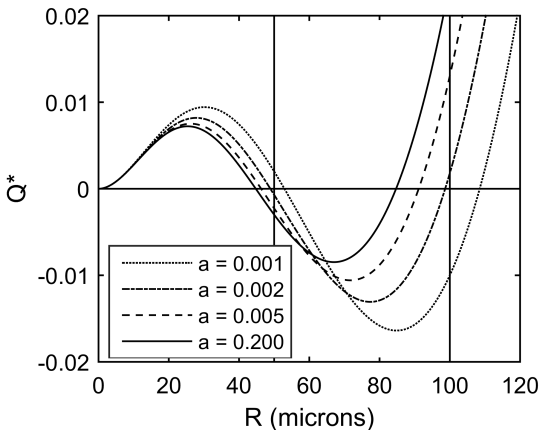

(b)

Figure 3.3: Effect of variation in peak width of size distribution on charge polarity, for non-dimensional charge $Q^* = Q(R)/4e\pi\sigma_0 R_1^2$. (a) Normalized particle size distribution functions $g(R)$ in the form of Equation (3.27), with $k_2/k_1 = 8$, $R_1 = 100\mu$m, and $R_2 = 50\mu$m. (b) Non-dimensional charge distribution functions corresponding to the size distributions in (a). Vertical lines at $R = R_1$ and $R = R_2$ provided as reference.

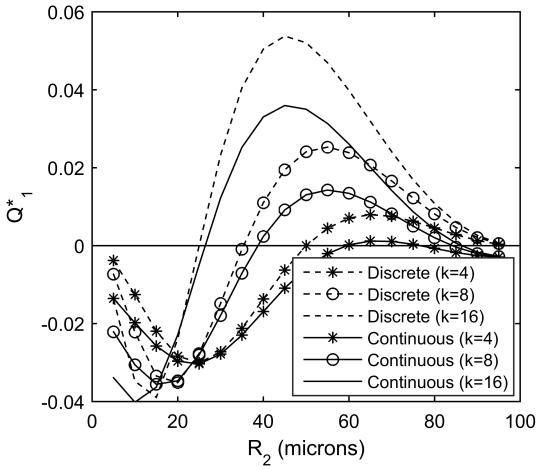

Figure 3.4: Non-dimensional net charge $Q_1^* = Q_1(R)/4e\pi\sigma_0 R_1^2$ on grains of radius $R_1 = 100\mu$m for a size distribution of the form of Equation (3.27), with $a = 0.005\mu$m. As the ratio of the peak heights (k) increases, the size ratio ($d = R_2/R_1$) below which large grains charge negatively decreases. Note that the charge predicted by the continuous distribution is very similar to that predicted by the discrete model, with some variation due to the effect of the nonzero peak width (as seen in Figure 3.3b).

existing experimental evidence could be attributed to a number of factors. The new polarity distribution is a result of the inclusion of area-dependent charge transfer because, when the area dependence is removed, the predictions made by the continuous distribution model closely match those of the discrete model. The fact that the polarity reversal in bidisperse mixtures often appears in between size peaks, where the number of grains present is comparatively very small, and that mass ratios are often unreported in experiments, make the polarity reversal difficult to observe. However, experiments on collisions of spheres suggest that the transferred charge is indeed proportional to the contact area [35, 46, 47], suggesting that our implementation of a contact area dependence is accurate. Additionally, small grains may have more irregular surfaces that do not transfer charge as we expect. Many grain charging experiments occur in atmosphere; some experiments have shown that

charging in vacuum or a neutral gas produces vastly different charge patterns [29], while others have suggested that humidity from the air adsorbed onto grains creates conductive paths during collisions that may alter the process of charge transfer [8, 16, 17, 18, 49]. These possibilities must be explored to determine what conditions are necessary in order to correctly predict grain charging.

In particular, the role of surface water in obfuscating experiment results cannot be understated. Prior experiments indicate that the presence of an electric field in a granular mixture can lead to charge exchange during collisions, leading to a self-reinforcing phenomenon in which the charge separation continues to grow with continued mixing [1, 18]. Zhang, *et al*, proposed a charge transfer mechanism entirely based on the motion of dissociated ions in the surface water layer on the grains, whereby the contact of two grains creates a conductive path across which these ions can move and leave net charge on each grain after separation [18]. This phenomenon may obscure the effect of contact-area-dependent charging processes that would otherwise dominate the charge transfer in dry environments like deserts and dusty airless bodies like the Moon. The fact that charging is known to occur in these dry environments, however, suggests that these models may still be accurate, although care must be taken to eliminate surface water when conducting experiments to compare to the models.

3.3.3 Predicted Charge Magnitude as Compared to Experiments

In Figure 3.2b, we saw that our new contact-area-dependent charge transfer model predicts a much lower charge magnitude than existing models for the same size distribution. In fact, it has been noted that even existing models underestimate the charge magnitude compared to grain charging experiments, leading to speculation regarding the validity of the trapped electron model in general [21]. We believe that the large difference in charge magnitude and the polarity reversal may be related to a single phenomenon ignored by the models. In particular, we suspect that the influence of atmospheric ions or adsorbed humidity encourages charge transfer in a manner that neglects the effect of contact area, as discussed in Section 3.3.2.3. This effect has been connected to increased charge separation in a number of experiments [8, 16, 29]. The fact that many experiments have been conducted in atmosphere or in the presence of other gases and have not involved pretreatment of the grains to eliminate adsorbed water suggests that this confounding factor may indeed be present, causing the results to diverge from the idealized case.

3.4 Notes on this Model

In the pursuit of a more realistic model for same-material granular insulator tribocharging, we have built upon Lacks and Levandovsky's original model and added size-dependent charge exchange and the ability to consider arbitrary size distributions, rather than discrete, bidisperse mixtures. The predictions made for continuous size distributions are similar to those made for discrete distributions of

a similar form. In the limit where the continuous distribution approaches a discrete distribution, the charge predictions converge. We have also modified the underlying model for charge transfer by including a dependence on contact area in determining the number of electrons transferred in each collision. This model predicts that mixtures of two size species with a smaller population of larger grains may display a reversed charge polarity (i.e., large grains charge negatively and small grains charge positively) compared to Lacks and Levandovsky's model. Leading theories on insulator charging suggest that charging in vacuum or under different humidity conditions may lead to different charging behavior, especially charge separation magnitude and polarity of final charge. We are designing an experiment to test the applicability of our model to granular tribocharging under various conditions, particularly in vacuum where the absence of humidity may cause contact area to play a more significant role. Future experiments will include pre-experiment baking of the grains to remove the adsorbed surface water, to ensure charging events are due to grain surface contact only. By experimentally testing for polarity reversal in a humidity-controlled environment, we hope to gain additional evidence in support of, or contradicting, the trapped high-energy model for triboelectric charging in insulators.

Chapter 4: Experimentation

This chapter contains material published in D. Carter and C. Hartzell, "Experimental methodology for measuring in-vacuum granular tribocharging," *Review of Scientific Instruments*, 90(125105), Dec 2019 [50].

4.1 Existing Techniques

Many common experimental tribocharging measurement techniques are unable to resolve individual grain charges, or correlate precise grain sizes to the measured charge. Instead, techniques using charged probes [13, 36, 51] or Faraday cups [30, 34] measure bulk charge polarity and/or magnitude of a particular subset of the tribocharged sample, then measure the size distribution of that subset. These methods are useful in measuring the degree to which charge is segregated by size, but do little to characterize the magnitude of that charge or its distribution within particular regions of the size distribution.

Another common limitation of existing experimental methods is the mechanism by which grains are charged. Some experiments fail to control for particle-to-container charging, causing the charge distribution to be significantly less representative of particle-to-particle charging, particularly when the container is made of a

different material [1, 30, 34]. In other cases, to avoid particle-to-container charging, the mixture is agitated by fluidization with a gas, sometimes air [1, 21, 30, 34, 44] or a presumably neutral gas like nitrogen [13, 36, 37, 38] or helium [29] to avoid influencing the charging process. However, experiments have suggested that the ambient atmosphere plays a large role in the magnitude and mechanism of charge separation, even for gases like helium and nitrogen [29]. Although little data exists on whether this influences the direction or relative distribution of charge within the mixture, it is known that the humidity of the ambient atmosphere does affect the charging process [8, 16, 17, 18].

There are experimental methods that provide the ability to correlate charge with grain size in a non-invasive way [44], but many still use charging methods that are influenced by atmospheric effects. We have adapted the high-speed videography methodology described by Waitukaitis and Jaeger [44] to conduct the tribocharging process in vacuum, minimizing the effects of container contact and atmospheric influence on the charging process. This method sends falling charged particles through a uniform electric field and observes their trajectories from a co-moving camera. As the experiment is conducted in vacuum, the effects of air resistance are eliminated, leaving only gravity and the electric force to act on the grains.

Our experiment differs from that of Waitukaitis and Jaeger in a few key ways. Primarily, the grains are kept in high-vacuum conditions throughout the charging and measurement processes. Although our operational pressure is not low enough here to ensure total elimination of adsorbed water from the atmosphere, we mitigate the effect of humidity by keeping the chamber sealed and under vacuum when not

in use, storing the grains in a sealed container with desicant packs, and maintaining an overall low-humidity laboratory environment. Future efforts could also include using lower pressures and/or preliminary high-vacuum baking of the grains before experimentation.

Additionally, we have designed our measurement and analysis software to measure individual grain diameters, rather than simply identifying large vs. small grains, to work for arbitrary size distributions. Although this experimental teststand was designed with silica beads on the 10^{-4} meter scale, it is applicable to a variety of granular mixtures with arbitrary size distributions with diameters as small as 10^{-5} meters, or even smaller with the use of higher magnification lenses. This also allows us to investigate the charging of complex mixtures like lunar regolith simulant.

4.2 Experimental Design

In our experiments, we have measured tribocharging in mixtures of zirconia-silica (ZrO2:SiO2) beads from Glenn Mills, Inc. Silica is known to undergo strong triboelectic charging and is the primary component of JSC-1A lunar regolith simulant. An accurate model for how zirconia-silica charges with itself will provide a strong foundation for a regolith charging model and for understanding triboelectric charge exchange in ceramics and other dielectrics in general. Most of the mixtures used consist of approximately 80g total of two sizes of beads, with radii sieved to $100\mu\text{m} \leq R_1 \leq 200\mu\text{m}$ and $200\mu\text{m} \leq R_2 \leq 300\mu\text{m}$. The two size fractions are mixed in various mass ratios of small to large grain species, denoted by m. Note that the

two sizes used are not from the same fabrication batch, and that subtle differences between them may contribute to charge exchange. Although this has significant implications for the accuracy of our modeling, the results of the experiment still validate the experiment's effectiveness as a measurement tool.

4.2.1 Physical Setup

A photograph of the experimental apparatus is shown in Figure 4.1. The design of this device was inspired by a similar mechanism by Jaeger, *et al* [21, 44], which was developed to enable individual grain charge measurements. However, we identified a few areas in which we could improve on this technique. First, the only place where they used a vacuum was in creating a 10 mTorr vacuum in the grain drop region, to eliminate air resistance on the falling grains. They charged their grains separately by fluidization with air, then poured them through a funnel into the measurement region. This additional handling, and especially the process of charging in atmosphere, likely influences the charging in ways that are difficult to predict and quantify. For this reason, we sought to conduct the entire experiment in vacuum, and to minimize handling or otherwise disturbing the grains between charging and measurement.

The other main way that we have improved the experiment is by reducing its overall footprint and automating much of the process. Their original experiment was 2.5 m tall and required weighting the camera carriage to overcome air resistance, using substantial padding to cushion the heavy carriage, and returning the device

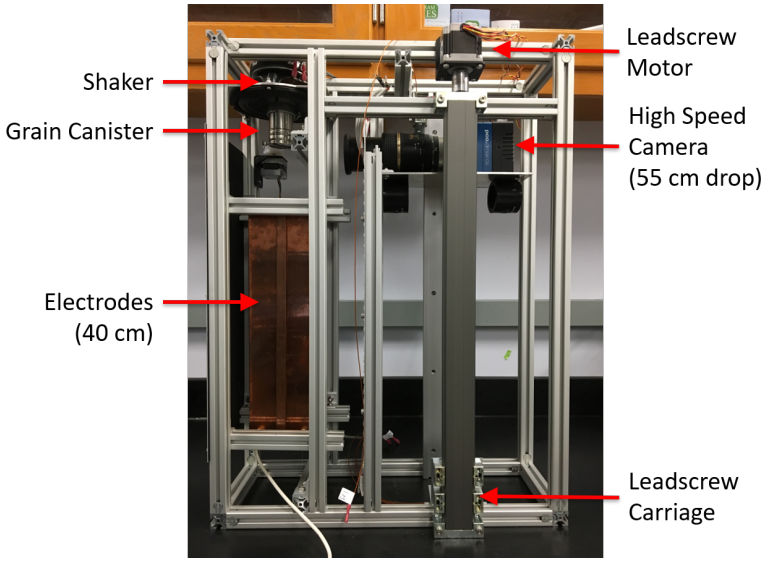

Figure 4.1: Experimentail setup. The device is designed to be placed in a vacuum chamber and operated at high vacuum. Grains in the canister are tribocharged via shaking and dropped through a region containing a transverse electric field. The camera is dropped and records the trajectories of the grains while both are in freefall.

to the top using a hoist. We sought a solution that could be implemented on nearly any lab desktop, and that could be operated with minimal manual oversight and intervention. The automation of the data collection and carriage return procedures expedites the process of data collection once a mixture has been brought to pressure.

4.2.2 Experiment Procedure

Experimental data collection is conducted in a sequence of four phases: sample preparation and vacuum pumpdown, introduction of triboelectric charge into the mixture, sample extraction and measurement, and reset of the experiment for further measurement. The inclusion of this final phase allows us to take as many measurements of the same prepared mixture as desired without breaking vacuum. The primary limiting factor in continued sample collection is the camera temper-

ature, as there is little to no heat dissipation from the camera by conduction or convection. For this reason, we are typically able to collect 5-8 videos of data for a single experimental run, each containing anywhere from 20-200 trajectories. In the following sections, we outline the design and operating procedure of our experiment.

4.2.2.1 Vacuum Chamber

Our experiment was designed to be compact and fit within our laboratory vacuum chamber. The influence of atmosphere on the charging process has been noted in prior experiments, so properly controlling this variable is essential to understanding the mechanism of charge transfer. The vacuum chamber used in this experiment is rectangular, with internal dimensions of 24" wide by 24" deep by 30" tall, and is shown in Figure 4.2a. The experimental apparatus is placed inside this chamber diagonally to allow the camera cables space to flex in the corner space without creating friction when the camera is dropped. A 21-pin electrical feedthrough allows signals to be passed into the chamber to the various motors and switches that control the experiment. The camera receives and transmits data through a separate multipin electrical feedthrough, and the high-voltage electrodes are also powered through a separate high-voltage feedthrough. These connections are all shown in Figure 4.2b.

When a granular mixture has been prepared and placed in the experimental apparatus, the chamber is sealed and evacuated. Pumpdown occurs in two stages. First, an Edwards XDS 15i scroll pump brings the pressure down to approximately 0.3 Torr, taking up to 30 minutes to reach this pressure. At this point the Leybold

(a) The 24” x 24” x 30” Kurt J. Lesker vacuum chamber housing our experiment.

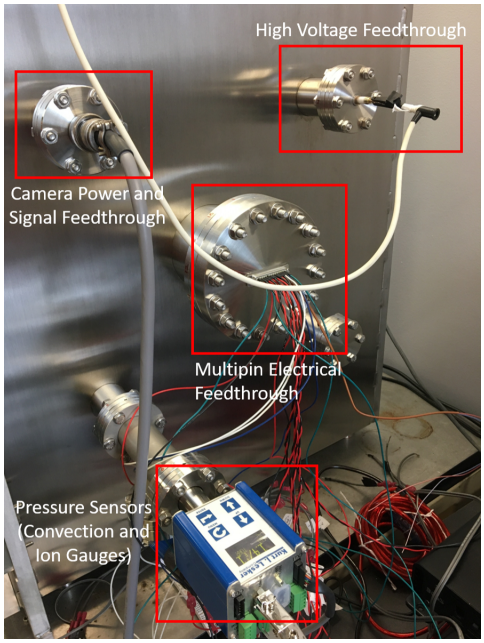

(b) Sensors and electrical feedthroughs for the vacuum chamber in which our experiment is housed.

Figure 4.2: Vacuum chamber configuration.

Turbovac 450i turbopump can be activated. Considering the humid environment in the Maryland area, and the inherent outgassing of many of the components in our setup, we have found that this pump can consistently reach pressures as low as 9 μTorr after one week of continuous operation, or 27 μTorr after approximately 16 hours. When operating this experiment, we prepare the chamber at the end of the workday and are able to collect data at less than 30 μTorr the following morning. These low pressures not only reduce the influence of atmosphere on the charging process, they are necessary to eliminate the drag force on the falling grains.

4.2.2.2 Grain Shaker

When the chamber has been evacuated to the desired pressure, the shaker can be activated. A picture of the shaker mechanism is shown in Figure 4.3. The grains are placed within a cylindrical steel canister made from a modified salt shaker. We have fitted a circular aluminum insert with a single hole into the canister, extending out through one of the many holes in the lid of the canister. As long as the swiveling lid covers this small hole, it presses against the hole to seal the grains in while shaking the canister, but when the lid is rotated, a narrow stream of grains falls through the opening. The diameter of the opening was chosen to be 5 mm to ensure that the ≤ 300 μm grains would fall without arching at the aperture, but would not pour so densely that the grains could not be easily distinguished or tracked.

Our model for grain-to-grain tribocharging requires that all charge transfer occurs between pairs of colliding grains, with minimal influence from collisions with the walls of the container. Other experiments and simulations have shown that grains allowed to mix within a container will experience significant charge segregation between the container walls and the grains, so electrically isolating the grains from the container walls is essential. To ensure that the only collisions in our canister occur between grains of the same material, we have coated the interior of the canister with a layer of zirconia-silica grains, essentially treating the mixture bulk as having an infinitely continuous boundary condition. Previous experiments using the same technique have shown this to be an effective method of preventing grain-to-wall charge transfer [44]. The grains are attached to the canister using a thin

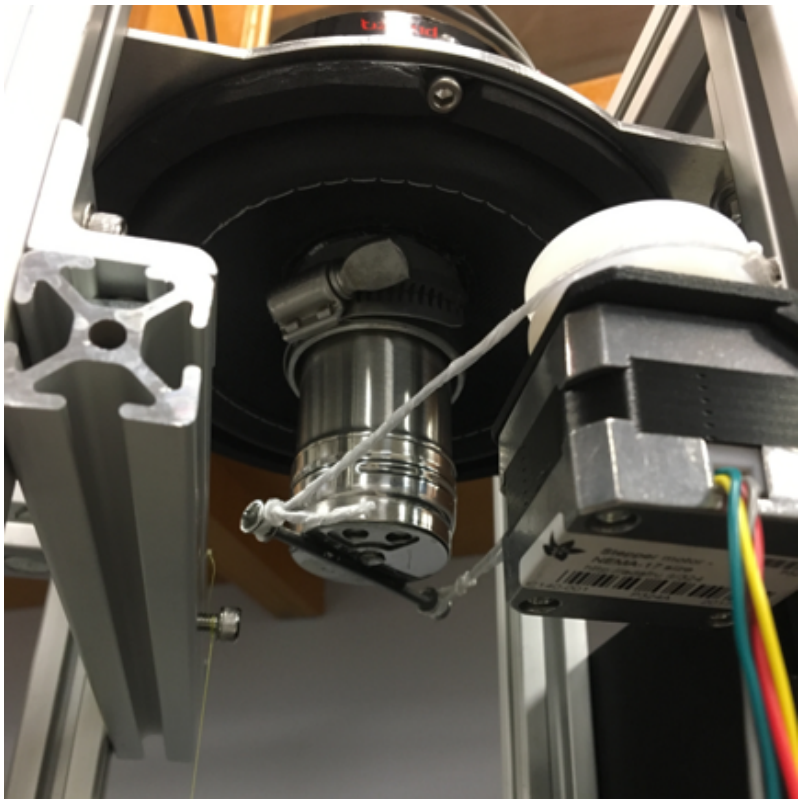

Figure 4.3: The grain shaker and sample release subsystem of our experiment. The central steel cylinder contains the granular sample and is attached to the vertically-mounted speaker. When the stepper motor at right turns, the lid is rotated, exposing the hole in the lid that is not blocked and letting a 5 mm stream of grains fall.

Figure 4.4: The canister in which grains are charged in our experiment. The interior of the canister has been coated with grains of the same material as those to be charged, so that no grain-to-wall charging occurs. When the lid is rotated during sample collection, grains fall through the 5 mm hole in the lid at bottom left.

layer polyurethane adhesive, onto which a fresh sample of grains is pressed until all gaps have been filled.

When the chamber has been pumped down to the operating pressure, as discussed in the previous section, the canister is vigorously shaken vertically to induce triboelectric charge exchange. The speaker is powered through a Boss 1100W amplifier, as shown in Figure 4.5a, to which we apply a waveform generated in LabVIEW. The interface for operating the speaker is shown in Figure 4.5b. Using this VI, we are able to control the frequency, amplitude (through the volume input), shaking duration, and shape of the waveform. In benchtop tests with a transparent con-

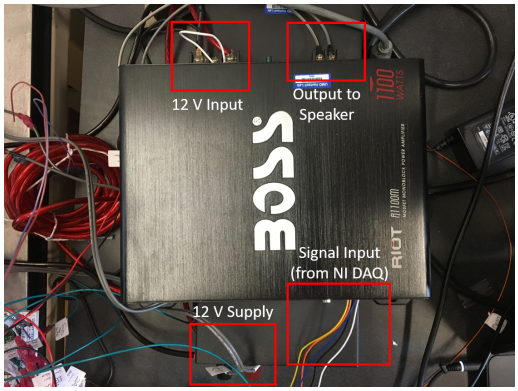

(a) Amplifier that interfaces with the shaker. Waveform data received as high-level inputs from LabVIEW UI via National Instruments Data Acquisition (NI DAQ) board and passed to the speaker.

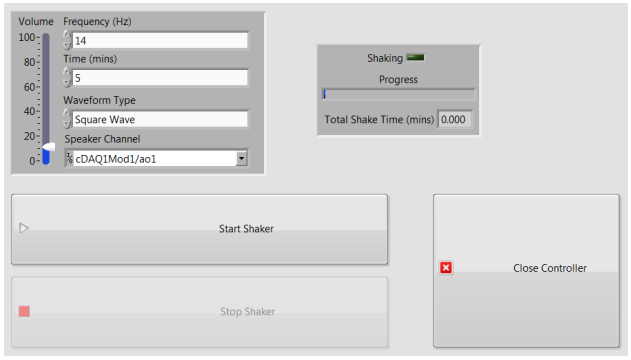

(b) Interface for controlling the shaker. User inputs the desired frequency, time, shape, and volume (amplitude) for the shaing waveform, then initiates shaking with the "Start Shaker" button. The indicators at top right track the total elapsed shaking time, persisting through stopping and starting where necessary. Pressing "Close Controller" aborts shaking and the VI entirely.

Figure 4.5: Shaker subsystem controller, external to the vacuum chamber.

tainer of the same size and weight, we have identified that with a square waveform at approximately 14 Hz, the height to which the grains are launched during shaking reaches a maximum, suggesting that this may be near the natural frequency of the system. At amplitudes that loft these grains near the top of the canister, the grains appear to be thoroughly mixed after cessation of shaking, exhibiting no apparent size segregation. To minimize the heat losses in the speaker during shaking, which can cause problems due to the vacuum environment, we set the volume slider to 10%, which limits the current through the speaker to approximately 1.5 A. The grains are then shaken continuously for 5 minutes, thoroughly mixing them and causing them to exchange charge.

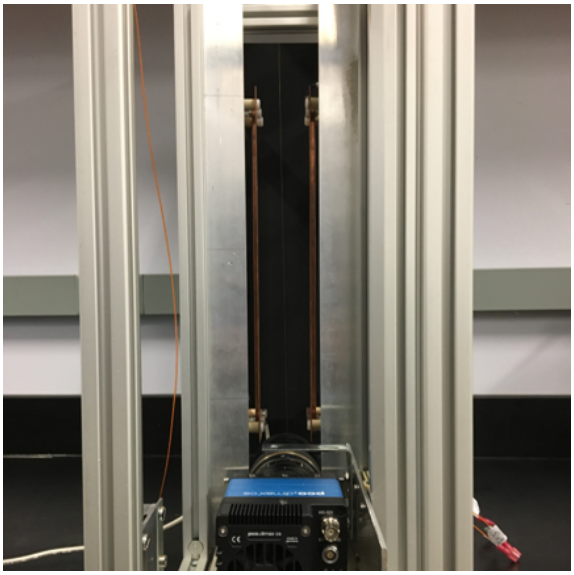

Figure 4.6: View of the parallel-plate electrodes, as seen from the camera (bottom). The background behind the electrodes is painted with an ultra-flat black paint to minimize backscattered light. Note the alignment string visible faintly between the electrodes.

4.2.2.3 Sample Release and Measurement

Once the grains are charged, the camera is turned on and the copper electrodes are charged to their operating potential of 4000 V. A head-on view of the electrodes as seen from the camera is shown in Figure 4.6 The electrodes are rectangular copper plates, each 110 mm wide, 400 mm tall, and spaced 60 mm apart. The electrodes are reinforced from behind with rigid copper bars to prevent bowing. The placement and height of these electrodes provide 170-200 ms per video in which the grains experience a consistent lateral electric force. Samples are taken from the canister by activating a stepper motor, as seen on the right of Figure 4.3.

The camera is a PCO Dimax CS3 high-speed camera, shown on its carriage in Figure 4.7. This camera is compact enough to fit in our chamber and is rated

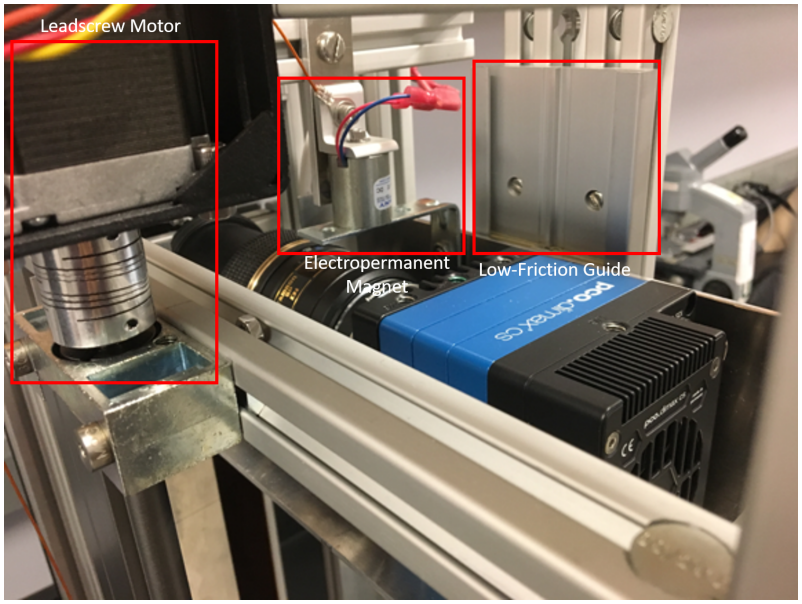

Figure 4.7: The camera carriage at the top of the experimental apparatus. The corner bracket (shown fixed to the electropermanent magnet) is attached to the carriage and is released from the magnet when collecting data, causing the carriage to fall along the low-friction guide rail.

for impacts up to 150 Gs. At the bottom of the carriage is a pair of circular rubber bumpers, which compress when the falling carriage hits the base of the vacuum chamber to absorb its kinetic energy and reduce the deceleration to an acceptable 20 Gs. The carriage is mounted on a low-friction rail, using a low-outgassing dry lubricant to minimize friction drag as the carriage falls. Extending horizontally over the top of the carriage is a steel corner bracket, which sits in contact with an electropermanent magnet at the top of the experimental apparatus, which operates as a reverse electromagnet. The magnet holds the carriage suspended at the top of the low-friction rail until a 12 V signal is applied, creating an opposing induced magnetic field that cancels that of the permanent magnet and allowing the carriage to fall.

We record video with a Tamron 1:1 macro lens at 1000 frames per second,

yielding a resolution of 11μm per pixel. Many lenses that give higher magnification are significantly longer, and although further magnification would improve the resolution of grain sizes, it would also dramatically reduce the length and number of trajectories captured. The frame rate was chosen to maximize blur reduction and trajectory length while ensuring sufficient illumination for resolving the images. At 1000 frames per second, most grains move no more than 1 mean grain diameter at any point along their trajectory, making it easier to track their motion across frames. This frame rate is also low enough that the grains can be illuminated sufficiently in this confined space to calculate their centers and approximate diameters. Illumination of the falling grains is performed by two banks of LED strips mounted on either side of the camera carriage track. Due to the compact nature of our test stand, there is limited available space for mounting lights; the lens and closely-spaced electrodes obscure the grains from most directions.

Sample collection and measurement is a time-sensitive process, and is automated entirely through the LabVIEW VI interface shown in Figure 4.8. Although the canister aperture is small, we would like to minimize the size of the extracted sample so that many runs can be conducted sequentially without significantly affecting the mixture. The canister must be closed shortly after data collection to keep from wasting samples. Furthermore, the camera does not have a low-power standby mode; once powered, the camera takes up to 30 seconds to boot up and then continuously reads data from the sensor until triggered to stream this data to storage. Because of the high-vacuum environment, this causes the camera, among other components like the LEDs, to heat up quickly unless depowered soon after

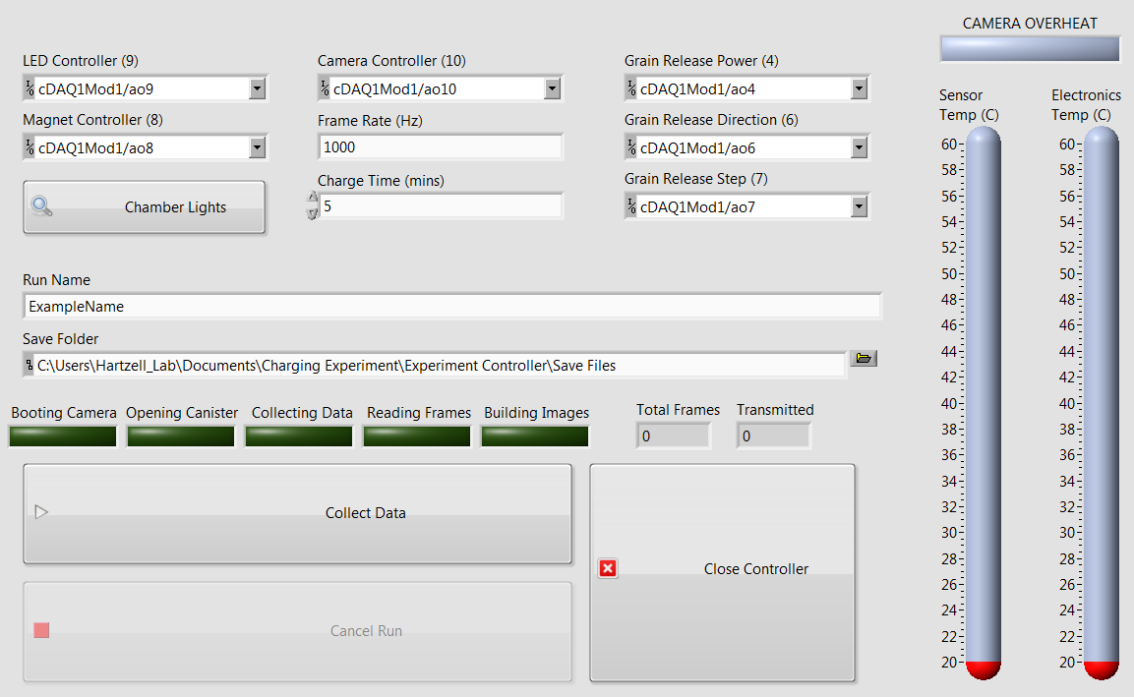

Figure 4.8: Virtual instrument (VI) for automating data collection. The user inputs the desired frame rate (default 1000 Hz), charge time (default 5 min), a unique name for the experiment, and the desired save folder. When these fields are complete, the "Collect Data" button becomes active, as shown. When the camera is plugged in and the "Collect Data" button is pressed, the system proceeds through the stages of data collection, constantly monitoring and displaying the camera's thermal status. If the camera begins to overheat or the user presses "Cancel Run," the system quickly closes the canister (if necessary) and aborts all processes, allowing the user to unplug the camera.

data collection is complete.

The VI prompts the user to input the desired frame rate and a descriptive name for the sample to be taken, as well as the time for which the sample was shaken. Once these fields have been completed, the "Run" button is enabled. Before beginning data collection, the user must plug in the camera to begin the bootup process and power on the high-voltage electrodes. When the "Run" button is pressed, LabVIEW polls the camera for its status for 30 seconds before aborting. If the camera becomes ready during this time, the system proceeds to prepare for data collection. First, the

camera is sent a set of commands to create the appropriate data buffers and set the region of interest, frame rate, and corresponding exposure time. When the camera is prepared for operation, the sample extraction stepper motor is activated, rotating 90 degrees so that the canister aperture is exposed and grains begin to stream down between the electrodes. As soon as the stepper motor stops, LabVIEW applies power to the LEDs and triggers the camera to begin recording, then applies power to the electropermanent magnet to release the carriage. The carriage falls alongside the grains, filming them in an approximately co-moving frame, before reaching the base of the chamber after approximately 0.6 seconds. After 1 second elapses from activation of the electropermanent magnet, LabVIEW tells the camera to cease recording, the sample extraction motor rotates the canister lid back into place, and the LEDs and electropermanent magnet are depowered. The camera continues to read out captured images to a single binary file until all files have been read, at which point the camera can be depowered.

In the final step of data collection, LabVIEW reopens the binary file containing all captured images and begins reading them out into individual TIFF images. Using the known image dimensions from the specified region of interest, segments of the binary file are read out into images until all images are created, then a brief readme file is created containing the region of interest, frame rate, and exposure time used to generate the data. In order to uniquely identify each video, a specific name is created for the folder and as a prefix for each image. This name consists of the parameters used to create the video appended together, such as "ThreeQuarter4kV_300s_1000Hz_Oct11_1307," which indicates that this video labeled Three-

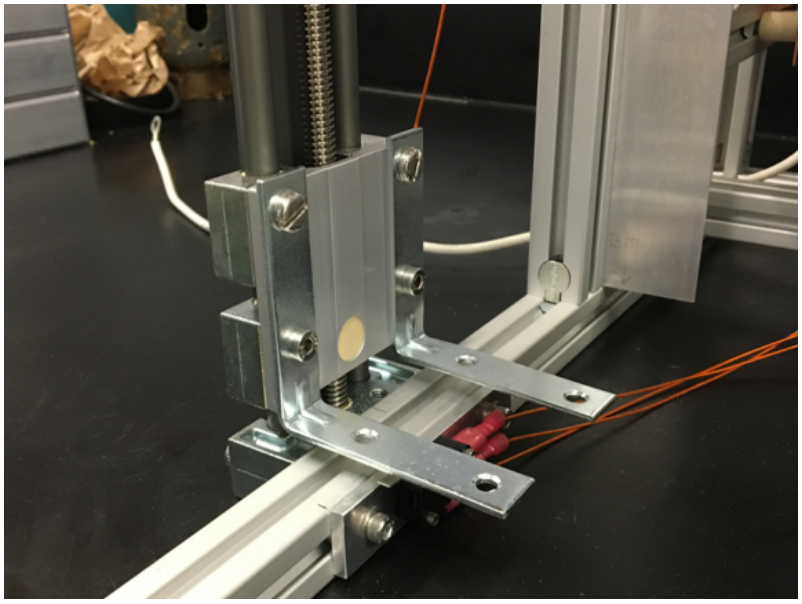

Figure 4.9: "Forklift" device for returning the camera carriage to the top after each experimental run. The leadscrew uses a dry lubricant to reduce both friction and outgassing, and is driven by a stepper motor at the top of the device. When the lift returns to the bottom, it activates a limit switch and stops.

Quarter4kV was created for a mixture shaken for 300 seconds and filmed at 1000 frames per second on October 11 at 1:07pm. This allows us to identify key parameters of the mixture at a glance and when reading the data in for analysis.

4.2.2.4 Carriage Return

Because the camera must fall to the bottom of the device to collect data, we must return it to the top without breaking vacuum to collect another set of data. We have accomplished this with a forklift-like mechanism attached to a leadscrew, which is moved up and down by a stepper motor controlled through a third LabVIEW VI. The forklift mechanism is shown in Figure 4.9. The forklift raises the carriage until the steel bracket reconnects with the electropermanent magnet, then moves back down to the bottom of the device where it won't interfere with the falling carriage.

This process can be automated using limit switches at either end of the leadscrew to put the carriage in place and return the forklift to the bottom of the device with a single button press. The bottom switch acts as a single pole double throw (SPDT) switch in the "normally closed" configuration, pulling the output voltage up only when actuated by the forklift. The top switch is closed when the corner bracket on the carriage makes contact with the electropermanent magnet, pulling its output voltage down when the camera carriage reaches the top; the conductive corner bracket is wired to the logic board's 5V rail, and the outer casing of the electropermanent magnet is also conductive, effectively creating a single pole single throw (SPST) switch between the two. These outputs are connected to the motor driver's direction pin through a logical OR gate, with a digital high moving the leadscrew carriage down; the leadscrew will always move upward unless only the top switch has been pressed. If using a LabVIEW analog or digital input board, the states of these switches can also be displayed, and the VI will check for the condition where either both switches are pressed or the bottom switch is being repeatedly opened and closed; these conditions indicate that the carriage has reached the bottom of the chamber.

4.3 Data Processing and Analysis

The collected data is processed in two phases. First, the images are passed through an algorithm to identify grain locations relative to the reference string, and manually inspected to add back missing locations and remove clumped and

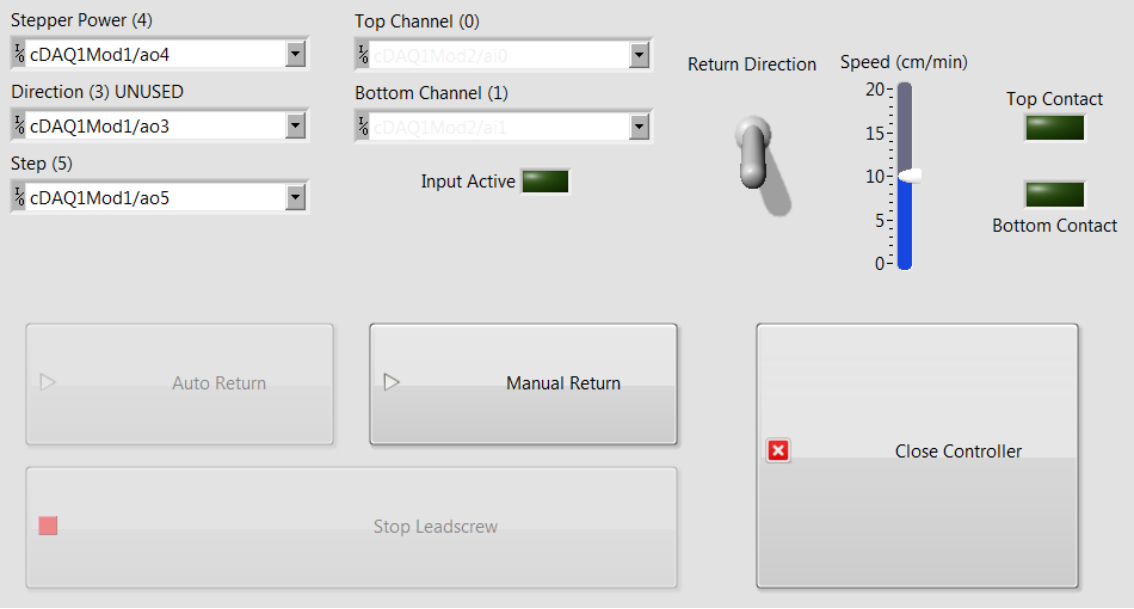

Figure 4.10: Virtual instrument (VI) for automating carriage return. When a National Instruments analog input board is connected, the "Input Active" and top and bottom contact indicators become active, and the "Auto Return" function is enabled. In manual mode, the user can input the desired return direction and speed (lower speeds provide additional torque when necessary).

poorly-resolved grains. These positions are linked together across frames, giving us an estimate for the acceleration, and charge-to-mass ratio, due to the electric field. Next, we determine and subtract out the background brightness from each image, leaving only the pixel values representing light reflected off the grains. The total of these values for a single grain is proportional to its cross-sectional area, giving us an estimate of the grain diameter, and therefore its mass.

4.3.1 Image Filtering and Grain Identification

Figure 4.11 shows a sample video frame obtained by applying a noise-reduction filter to the raw data. The method we use for identifying and tracking particles was developed by Crocker and Grier [52]. We apply a band-pass filter to identify objects

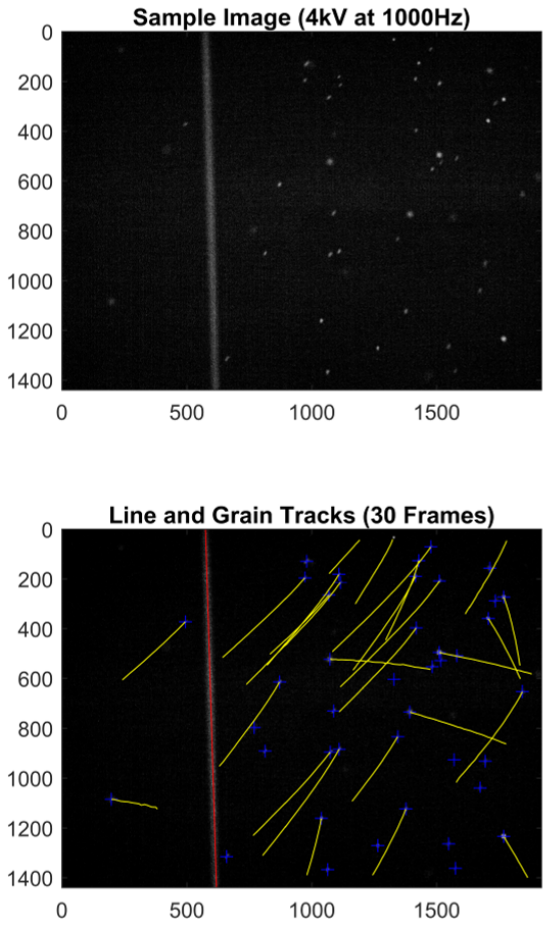

Figure 4.11: Sample frame, with and without features overlaid. At top, the noise-reduced frame alone. At bottom, the same frame with grain locations (blue crosses), string center (red line) identified. Grain trajectories (yellow arcs) are shown for the 30 frames following the one shown. Units are pixels.

of a specified size, which we will refer to as a "standard diameter." For the sample mixture discussed here, grains have diameters ranging between 100 and 300μm, so we use a standard diameter of 25 pixels, or approximately 280μm. This value was chosen because the algorithm works best when the standard diameter is only slightly larger than the objects to be found, and the distribution of observed grain sizes trails off at approximately 270μm. After applying this filter, the result is then rescaled to a value out of 255.

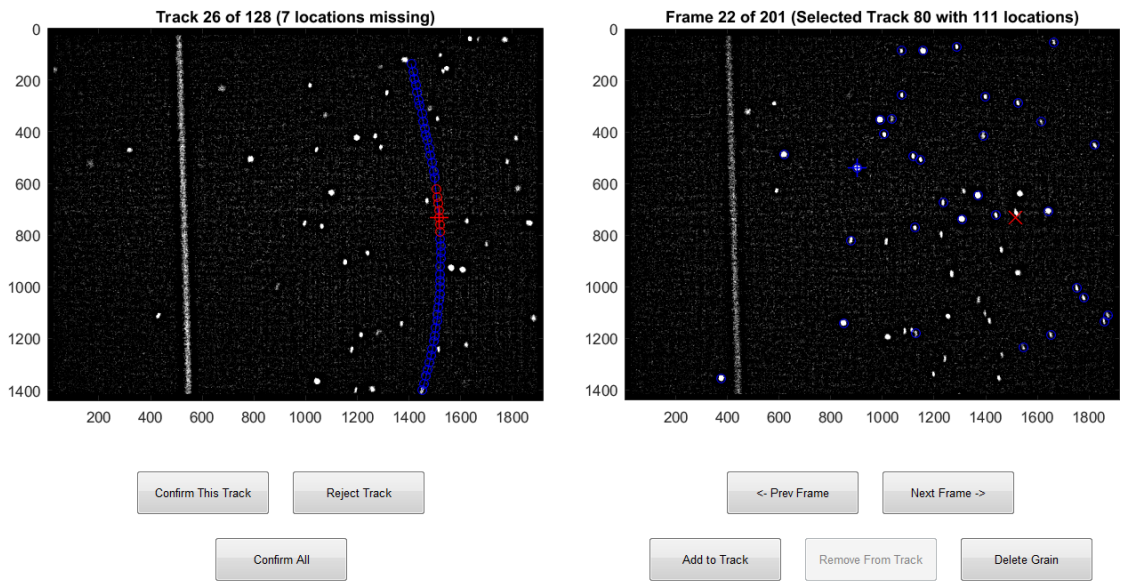

Figure 4.12: Interface for editing tracks found by the tracking algorithm. Tracks are presented sequentially in the left window, and possible grain candidates are presented in the right window. The user can navigate through each frame and add or remove any grains to the track. Estimates for possible missing locations are presented based on the calculated trajectory. Units are pixels in source images.

Two prominent features remain in the filtered image: the alignment string, and the grains themselves. To find the string, we locate its center on the image's central horizontal row of pixels, then move toward the top and bottom of the image, estimating the center along each row of pixels. These locations are used to calculate a linear fit to the string, providing a reference to the camera's minute variations in roll and yaw as it falls. The grains are found by identifying all local brightness maxima within a radius of a standard diameter. These estimated centers are refined by finding the centroid of the pixel values in the vicinity of each point. This reduces the influence of residual noise or asphericity on the identified center, but can cause additional errors when two grains overlap or collide.

4.3.2 Trajectory Determination

The grains are accelerated laterally by the electric field, and many also have some small non-zero vertical velocity relative to the camera. The trajectories formed by these grains from image frame to image frame can be analyzed to determine the charge-to-mass ratio of each grain. To construct these trajectories from the raw image data, we find the least-mean-square displacement of all pairings of grains with their nearest neighbors across each pair of frames, assigning a unique track number to each set of positions. From the sample video described in Section 4.2, this process identifies 402 trajectories, many of which are simply individual unpaired grains; 125 of these contain at least 10 frames, for which the average length is 42 frames.

The filters in the previous section have a tendency to miss a small percentage of the grains that do not meet the brightness threshold, causing some tracks to be divided in two or more segments. This is exacerbated in the later frames as grains gain speed, and may move so fast that their motion between frames exceeds the maximum for tracking. These effects inflate the number of valid trajectories found. Furthermore, while actual collisions between grains appear to be rare, close crossings do happen on occasion. When they do, only the brighter grain is identified, and one trajectory sometimes incorrectly continues with the wrong grain. Even if these events are correctly flagged and rejected, the remaining tracks are primarily incomplete, and it is advantageous to manually inspect and correct them to obtain accurate trajectories. Frequently, two or or more grains adhere together, typically

a small and large grain but occasionally creating a large clump of many grains. The algorithm often identifies this clump as one or more grains, but the size and acceleration of its components are not usable data. These points also must be rejected before processing the data.

We have developed an interface for examining and manually correcting trajectories by adding or removing grains, searching for grains that were missed due to overeager filtering, and deleting poorly-resolved objects like overlapping grains or residual background noise. Each track is presented as a set of connected points, as in Figure 4.12. The user can navigate from frame to frame using the "Prev Frame" and "Next Frame" buttons, and each grain location is presented in each frame as a candidate to be added, removed, or deleted using the corresponding buttons. In addition, the interface allows for manually selecting regions that clearly contain grains that were not identified by right-clicking. These grain locations can be added back to the frame, enabling the reconstruction of long grain tracks that would have otherwise been lost. With this method, we are able to condense the 402 trajectories into 128, with 118 having at least 10 points and for which the average length is 54 points.

The acceleration due to the Lorentz force can now be calculated for each grain trajectory by applying a second order polynomial fit. The forces that dominate the motion of the grain here are the gravitational force $F_g = m\vec{g}$ and the Lorentz force due to the electric field, $F_E = q\vec{E}$. (Note that the string appears significantly angled away from vertical in our videos; this is due to the uneven floor in our laboratory, but can be corrected.) We define $\hat{h}$ to be the horizontal unit vector orthogonal to the

direction of the gravity vector $\hat{g}$ and parallel to the camera's focal plane. Calculating the angle ϕ_{vert} of the string from the vertical, such that $\hat{g} \cdot \hat{E} = sin\,(\phi_{vert})$, we find that the net force acting in the direction of $\hat{h}$ is $F_h = ma_h = q\vec{E} \cdot \hat{h} = qEcos\,(\phi_{vert})$.

To determine the quantity $\frac{q}{m}$ from this expression, we calculate the positions of each point in a trajectory along the $\hat{h}$ basis vector. For each point in the trajectory, we calculate x_h, the normal distance of that point to the string center. This corrects for both the nonvertical gravitational vector and the camera's yaw and roll, which would otherwise introduce significant errors. We then apply a second order polynomial fit to the positions, with the known elapsed time $\Delta t = 10^{-3}$s between each frame. The second-order coefficient a_{fit} is the acceleration orthogonal to gravity, such that $ma_{fit} = qEcos\phi_{vert}$. The root mean squared residual of this fit is denoted here as Δ_a and recorded for each trajectory.

4.3.3 Size Determination

In order to use this experiment to measure charge segregation in arbitrary mixtures with continuous size distributions, it is not sufficient to roughly categorize grains as "large" or "small" based on a cursory analysis of the images, as is frequently done in other granular tribocharging experiments. Instead, we have developed a technique for estimating an individual grain's diameter from the images. The method we use assumes that the total light B reflected from a grain of diameter D onto the camera sensor is proportional to the grain's cross-sectional area. As our grains are nearly spherical and have diffusely reflective surfaces, this should provide

a reasonably accurate estimate of the size. We can then determine the diameter D from the expression

$$D = C\sqrt{B} \tag{4.1}$$

for some empirically-determined scaling constant C. The brightness B is found by summing the values of the pixels making up the grain in a particular image. The constant C is measured for each material by placing a sample of grains on a microscope slide, placing it in the experimental apparatus where the grains would be, and taking a high-speed video of the slide under normal operating lighting conditions. The slide is then examined under a microscope (see Figure 4.13), where the actual spherical diameter of each grain can be determined. The background brightness, which has a mean pixel value of approximately 20-25, is subtracted out to give a mean-zero background level, and the pixel values in the vicinity of each grain are summed to determine B. We can then find the average value of $\frac{R}{\sqrt{B}}$ among all grains, which becomes our scaling constant C.

A major challenge we face is the prevalence of "motion blur" in our images. When filming these grains at 1000 frames per second, our camera has an exposure time of $\Delta t = 944\mu$s. Some of our smaller grains can reach speeds that cause them to travel upwards of 20-30 pixels between frames in that time, causing them to appear elongated along their direction of motion. Our sizing method is resilient to blurring, as the window around each grain is large enough to include all photons reflected onto the sensor by the grain regardless of its speed or level of focus, but blurry grains do

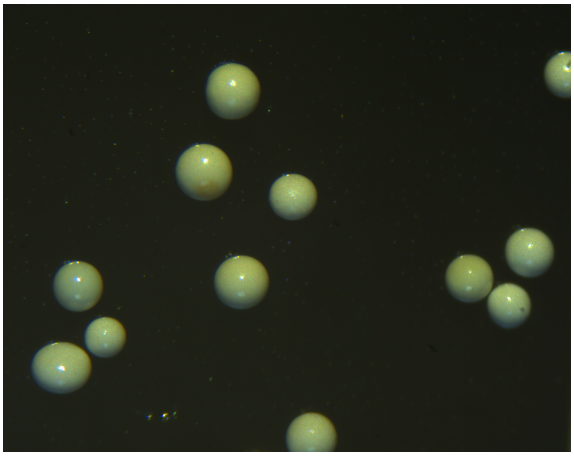

Figure 4.13: Large size fraction of zirconia-silica grains (diameters 200 μm to 300 μm) under microscope. Grains are highly spherical with uniform smooth surfaces, with a few exceptions.

present a challenge for identifying and removing the non-zero-mean background.

4.3.3.1 Sizing Procedure

First, we must remove noise from the image that originates from current leakage in the camera sensor. Known as "dark current", this is a function of the camera itself and can be found and corrected by taking a video without any illumination (e.g., with the lens cap on). The frames of this dark video are then averaged together on a pixel-by-pixel basis to create an average frame representing the dark current. This is then subtracted from each frame of our video. Next, we determine the mean remaining background pixel value. A mask is applied to each frame that selects only regions more than a standard diameter away from the string or any grain, and the mean value of these pixels is calculated. This value is the mean value of the background due to ambient light, and subtracting it from each frame ensures that for any box drawn around a single grain, the total value of the contained pixels

represents only the light reflected by the grain itself.

We then determine an appropriate window around the grain in which to calculate its brightness. The width of this window is 1.5 standard diameters and is centered on the grain to be measured, ensuring that the entire grain is enclosed without being so large as to include other nearby objects. This subset image is then extracted, such that the center of the subframe (x_s, y_s) is centered on the grain's location (x, y) in the frame. Next we check that the grain fits within this window. We identify the trajectory to which the grain belongs, and estimate its velocity $v = (\dot{x}, \dot{y})$ at the location in question. The grain's displacement is then calculated as $(\Delta x, \Delta y) = (\dot{x}\Delta t, \dot{y}\Delta t)$ pixels. If the dimensions of the window are not larger than this displacement plus a standard diameter, we cannot be sure we have fully captured the grain, and this location is rejected. Otherwise, sizing is done by summing the pixel values contained in the subframe and applying the conversion from that value B to the grain diameter D defined by Equation 4.1.

Finally, because many of the grains are slightly out of focus or highly elongated, we manually compare the average diameter of each grain trajectory to the images of its positions. Some of these require manual correction, and some are too poorly resolved to be confident in the results obtained. After all grains have been confirmed, the results are saved and charge determination can begin.

To obtain an estimate for the uncertainty involved in this method, we return to the calibration images described in Section 4.3.3. We apply this sizing algorithm to the images taken under experimental conditions, obtaining a set of diameter estimates D_{calc}. These values are then compared to the corresponding sizes as

determined under microscopic analysis, and the root mean square residual is found for each size species. We have measured a root mean square residual for diameter measurements of 8.1 μm and 8.4 μm for small and large size species, respectively. Henceforth we assume that each individual diameter measurement has an associated uncertainty of $\Delta_D = 8.4\mu$m. To ensure that this method is robust enough to handle blurry and in-focus grains, we took a series of ten images using a single slide to which grains had been attached, placing it at varying distances from the camera lens. We found that, as long as the mean background brightness level was correctly calculated, this method achieved the same accuracy regardless of blurriness.

4.3.4 Calculation of Grain Charges

Given the measured grain size and grain acceleration, it is possible to derive the charge on an individual grain. From the grain's acceleration fit $a_{fit} = \frac{q}{m}$, the estimated diameter D_{est}, the material density ρ, and the electric field strength $E = \frac{V}{L}$, the charge q can be expressed as follows:

$$q = \frac{ma_{fit}}{E} = \frac{\pi\rho L D_{est}^3 a_{fit}}{6V} \tag{4.2}$$

In this setup, we have applied a voltage of $V = 4$ kV to the parallel plates, with a spacing of $L = 60$ mm between them. These charge measurements are subject to a few significant sources of error, the largest of which by far are the uncertainties in a_{fit} and D_{est}. Here we assume that these uncertainties are significantly larger than errors in the applied voltage, which we have found to be accurate to less than 1%

variation, and in the infinite parallel plate model for the electric field.

The uncertainty associated with the charge q can therefore be expressed as a combination of the uncertainties Δ_D and Δ_a as follows:

$$\Delta_q = q\sqrt{9\left(\frac{\Delta_D}{D}\right)^2 + \left(\frac{\Delta_a}{a_{fit}}\right)^2} \tag{4.3}$$

A sample plot of charge measurements is given in Figure 4.14. Vertical error bars are given by the acceleration fit uncertainty Δ_a, and horizontal error bars are given by the sizing uncertainty Δ_R. These results include 128 trajectories collected from four camera drops. We have plotted the charge-to-mass ratio rather than the total charge as the former is determined from the acceleration a_{fit} and independent of the size measurements. Note that the large grains carry a negative charge, while the small grains are charged positively. This is a reversal from the trends observed in most previous experiments, where the smaller grains tend to charge negatively and the large are positive. This polarity reversal, with small grains charging positively, agrees with predictions of our semi-analytic model [45] and is consistent across experiments on different days and with different mixture ratios. We propose that this charging polarity was not observed in prior experiments due to contamination of prior experiments via atmospheric effects and/or charging other than grain-to-grain charging.

Although the tested size distribution is not entirely discrete, it is useful to examine these results in terms of large (greater than 200μm) and small (less than 200μm) grains. We observe that the small grains have a mean charge-to-mass

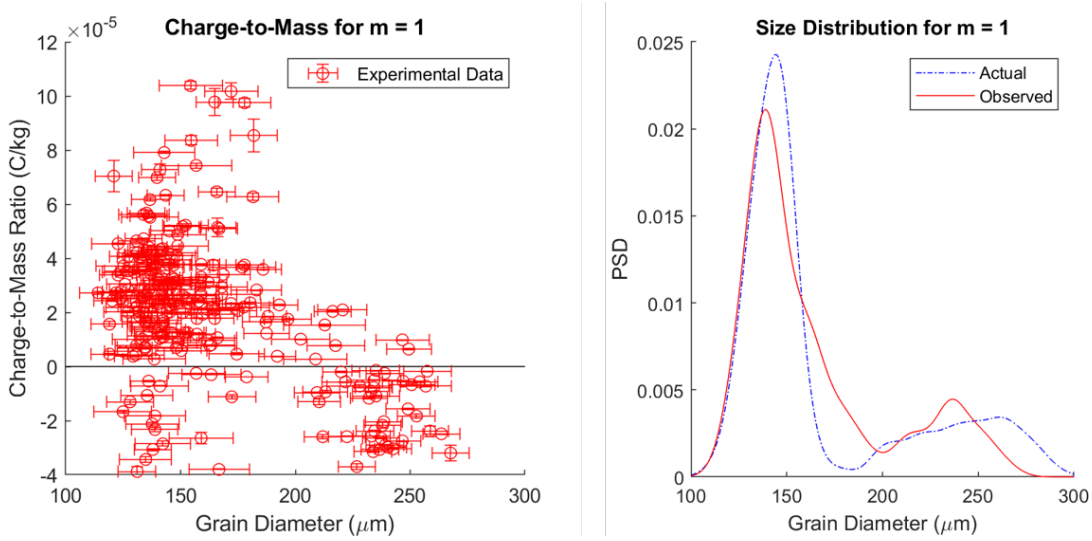

Figure 4.14: Results of experimental analysis of 1:1 (by mass) mixture of small (100-200 μm) and large (200-300 μm) spherical silica beads. The distribution of observed grain sizes from experiment videos is compared (at right) to the actual distribution as measured under microscope.

ratio of $(3.22 \pm 2.64) \times 10^{-5} C/kg$, whereas the large grains have a mean charge-to-mass ratio of $(-2.33 \pm 1.21) \times 10^{-5} C/kg$. Including their calculated diameters and associated uncertainties, we find that the small grains have an average charge of $q_S = (1.17 \pm 1.09) \times 10^{-13} C$ and the large grains have an average charge $q_L = (-5.34 \pm 2.33) \times 10^{-13} C$. Note that the large error bounds on these values are only in part due to measurement uncertainties; granular tribocharging is a stochastic process that results in a wide spread in charge for a single species, as in Figure 4.14, and this is reflected in the error bound on the mean charge.

To verify that this charging is due solely to grain-to-grain charge exchange occuring in vacuum, we have conducted tests using the same mixture and experimental conditions, but without activating the shaker. In this experiment, we found that the small grains measured carried an average charge of q_S $(9.03 \pm 68.3) \times 10^{-15} C/kg$, and the large grains carried an average charge of q_L $(-5.35 \pm 12.2) \times 10^{-14} C/kg$. The

mean charge on each species without shaking was at least an order of magnitude less than after shaking, suggesting that the majority of charge exchange does indeed occur in vacuum. We also note that the variance of the charge around the mean is significantly larger than the mean itself, indicating that there is little evidence of any significant correlation between size and charge polarity before shaking. We attribute the presence of what little charge is present to charge exchange during transport and preparation of the grains, but we remain confident that the dominant mechanism creating the charge segregation observed is granular tribocharging in vacuum.

Chapter 5: Experimental Results

The granular mixtures described in this chapter are composed of two size fractions of zirconia-silica (ZrO_2:SiO_2) beads from Glenn Mills, Inc. The size distribution measured for each component is shown in Figure 5.1. Each mixture described in this chapter is created by measuring out masses m_1 and m_2 of the larger and smaller components, respectively, and combining them. This mixture is then described by its mass ratio $m = \frac{m_2}{m_1}$.

5.1 Charge Exchange Models

Before presenting the collected data, we will first outline a set of models that are based on the continuous size distribution framework described in Chapter 3. We will compare these models to the observed charging phenomena to assess their relative accuracy and draw conclusions about the nature of triboelectric charge exchange. These models represent a variety of mechanisms previously proposed for the triboelectric charging of same-material dielectrics.

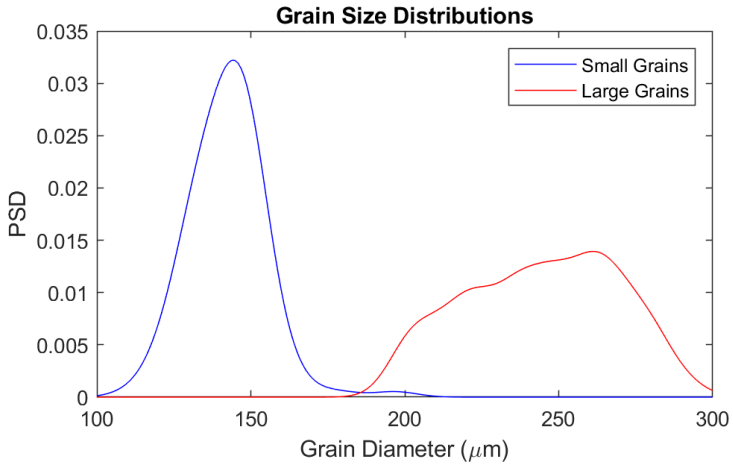

Figure 5.1: Size distribution of small and large mixtures, as measured under microscope.

5.1.1 Inelastic Deformation

In Chapter 3 we proposed that charging was due to high-energy electron transfer [45], where the charge exchanged in a single collision between grains of radii R_i and R_j is proportional to the contact area A_{ij} formed by Hertzian deformation of their surfaces. We represent this mechanism in the model labeled "Hertz." It has been observed that larger spheres and flat surfaces exchange charge proportional to their surface area in contact during even a single impact [46]. This model attempts to capture this phenomenon by describing the maximum contact area in common between two grains that deform due to their kinetic energy at the point of impact.

5.1.2 Constant Transfer

In our initial discussion of same-material charge transfer, we noted that many early models simplified the collision model by assuming that each collision transfers a fixed number of electrons [11]. The Hertz model we proposed as a replacement

relies on the assumption that the grains collide with enough energy to experience appreciable deformation. Theoretically, the actual energy and elastic modulus divide out, and only the relative contact area in the space of possible grain pairs is necessary to calculate the charge distribution. Realistically, the low collision energies and small size of the grains may result in deformations so small as to provide very little difference in charge transfer among sizes. In this case, the Hertz model would simplify to the constant contact area model. We have therefore included this model, labeled as "Constant," as a point of comparison to other models.

This model remains suspect for the same reasons mentioned in Chapter 3, and most models today suggest that the quantity of transferred charge is a function of the sizes of the two grains. However, we have included it here for the sake of completeness. It also serves as a reference point for the degree to which collisions cause charge to segregate by size.

5.1.3 Combination of Size and Material Differences

While we have assumed up to this point that the two size fractions of grains that make up our mixtures are chemically identical, the possibility exists that there may be small material differences that provide an alternative size-dependent transfer mechanism. The two size fractions were obtained pre-sieved from Glenn Mills, Inc, and it is unknown whether they came from the same production batch. While batches should be roughly identical, it is prudent to include a model that takes into account material-dependent transfer. This model is denoted as "CombofX",

where $f = X$ is the factor by which material transfer dominates over size-based transfer. Both mechanisms are based on the "Constant" model described above, but the number of transferred charges is X times larger if moving from a grain smaller than some diameter D_{mid} to a grain larger than that size. Here we have chosen $D_{mid} = 185\mu$m.

5.1.4 Exponential Decay

Other models for electron transfer have proposed that any electron is capable of transferring between contacting grains through tunneling [25]. Jaeger, *et al*, attempted to measure the density of high-energy electrons on zirconia-silica grains and determined that the number of transferred charges far exceeds the available population [21]. If "regular" electrons are also able to transfer simply by tunneling, this could explain the discrepancy between these observations.

Our model of this phenomenon is simplified for ease of application to our framework. To determine the number of charges transferred from one grain to another, we consider a single point on the surface of the first grain and find its minimum distance r to the surface of the second grain, as shown in Figure 5.2. The probability that an electron at the first point would transfer across to the second grain is then proportional to e^{-kr}. Assuming this point has area dA and contains σdA electrons, we can then integrate this value over the surface of the first grain that is able to "see" the second grain, giving the average number of electrons transferred in a single collision. While this is intended to represent electron tunneling, it can

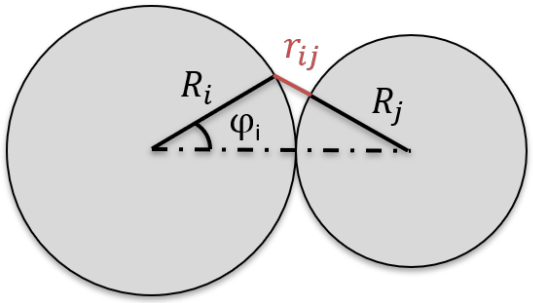

$$P(R_i, R_j, \varphi_i) = ce^{-kr_{ij}}$$

$$\Delta\sigma_i = \iint \frac{P(R_i, R_j, \varphi_i)\sigma_i dA_i}{4\pi R_i^2}$$

Figure 5.2: Diagram illustrating the exponential decay model. For each point on the surface of grain i with area dA_i, the probability of transfer P is multiplied by the number of charge carriers $\sigma_i dA_i$. The total number of transferred charges per collision is found by integrating $P\sigma_i dA_i$ over the entire surface of grain i.

also represent the transfer of positive "holes."

5.1.5 Total Surface Area

Some experiments have suggested that the presence of an adsorbed layer of water from the environment has a significant effect on the polarity and magnitude of the charge distribution. In many such models, ions dissolved in the water layer are able to transfer to the contacting surface, facilitating charge transfer on the surfaces of dielectrics where charges would otherwise be immobile. We have created a simplistic representation of this model, labeled "SurfA," in which the available contact area is equal to the entire surface area of the grain.

5.1.6 Collision Models

When determining the rate at which a grain collides with its neighbors, we must first determine the relative speed v_r with which it travels in the mixture. If collisions occur infrequently, and therefore the grain has only the speed imparted

to it when launched by the moving canister, our initial assumption may hold, but when collisions are frequent, the grains are more likely to redistribute their energy. Additionally, many regions of the mixture do not experience anything like the idealized ballistic collision model, instead experiencing inelastic collapse in which the grains encounter the rising canister floor and lose all their energy in a large number of rapid collisions. We have included two models in our analysis that treat the grains as conserving their speed, as initially assumed, and their energy.

5.1.6.1 Constant Velocity

In models denoted by the term "ConsV," we apply our initial assumption that all grains move through the mixture at approximately the same relative speed v_r. The shaker is mixed by vigorously shaking it vertically using a square waveform, causing all grains to be launched upward at the same time. At this point, they all have the same speed: that of the bottom of the canister on the upward stroke. This form of the model captures the collision rates as they occur at this point in time.

5.1.6.2 Constant Energy

As the launched grains collide with their neighbors, and especially as they move side to side, they quickly redistribute kinetic energy such that each grain takes on approximately the same energy E_0. In models denoted by the term "ConsE," we calculate a grain's approximate relative speed relative to the bulk as $v_r = \sqrt{\frac{2E_0}{m}} \propto R^{-\frac{3}{2}}$. Because constant multiplicative factors in the relative speeds divide out in calcu-

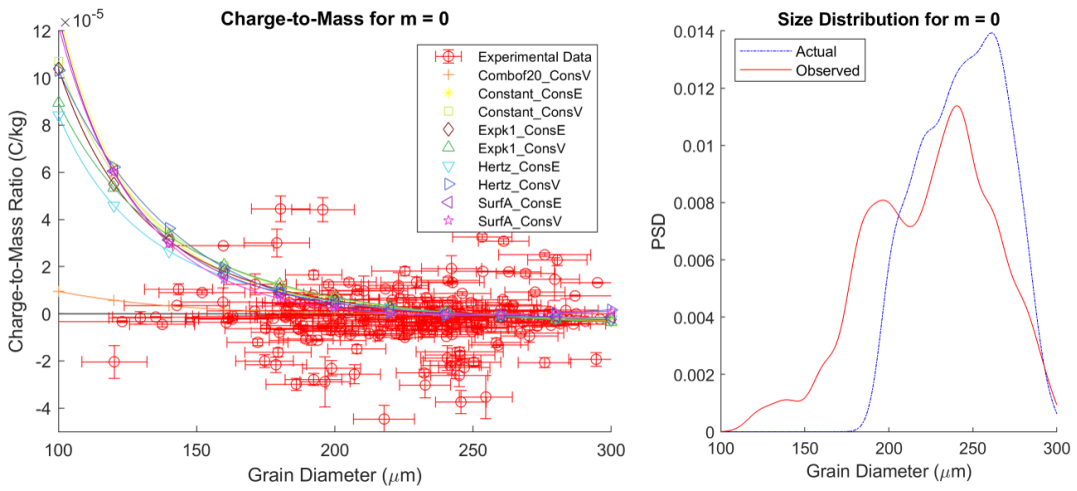

Figure 5.3: Results for mixtures composed entirely of large grains. Note the high variance in the measured charge-to-mass ratio compared to the mean value. For this nearly monodisperse case, little charge segregation occurs based on size.

lating the charge distribution function, only this relationship to R is relevant. This form of the model may better describe the collisional behavior in this experimental setup.

5.2 Results

The results for mixtures with mass fractions $m = 0, \frac{1}{8}, \frac{1}{4}, \frac{1}{2}, \frac{3}{4}, 1$, and 2 are shown in Figures 5.3, 5.4, 5.5, 5.6, 5.7, 5.8, and 5.9. A clear segregation of polarity according to size can be observed, with small grains charging predominantly positive and large grains charging negatively. Furthermore, as expected, the stochastic nature of charge exchange causes a wide variation in charge magnitude, and even polarity to an extent, at each grain diameter in the mixture. However, clear trends in polarity and magnitude, and especially their variation with both diameter and mass fraction, can be observed.

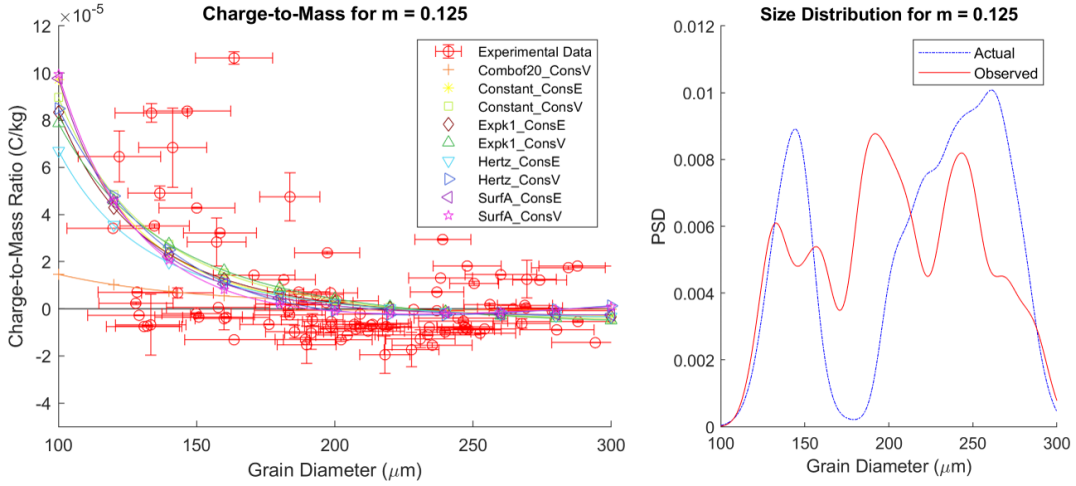

Figure 5.4: Results for mixtures composed of 1:8 small to large grains, by mass. Note the irregular shape of the observed sizes; this is due to the lower quantity of data relative to other size fractions. When the number of large grains increases, many small grains adhere to them while falling, so fewer clean trajectories are observed.

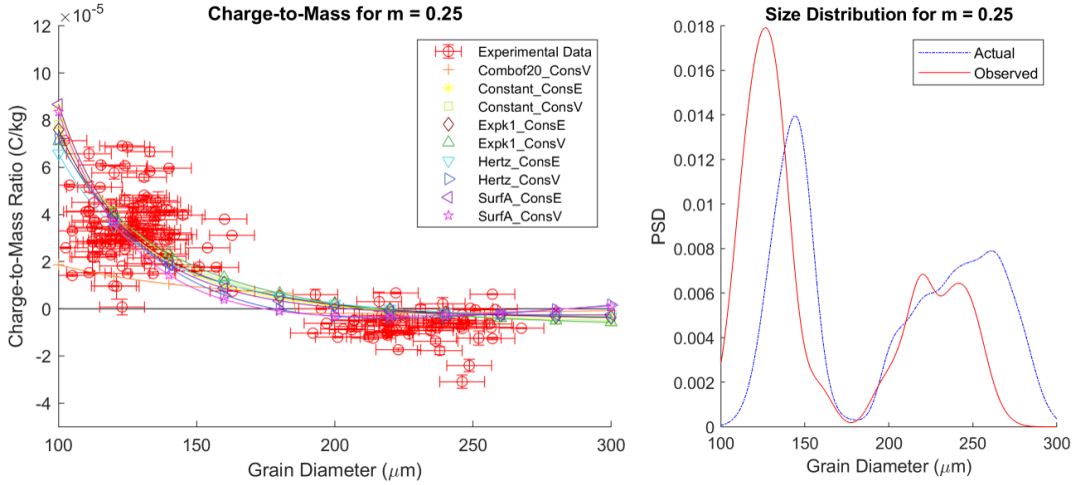

Figure 5.5: Results for mixtures composed of 1:4 small to large grains, by mass.

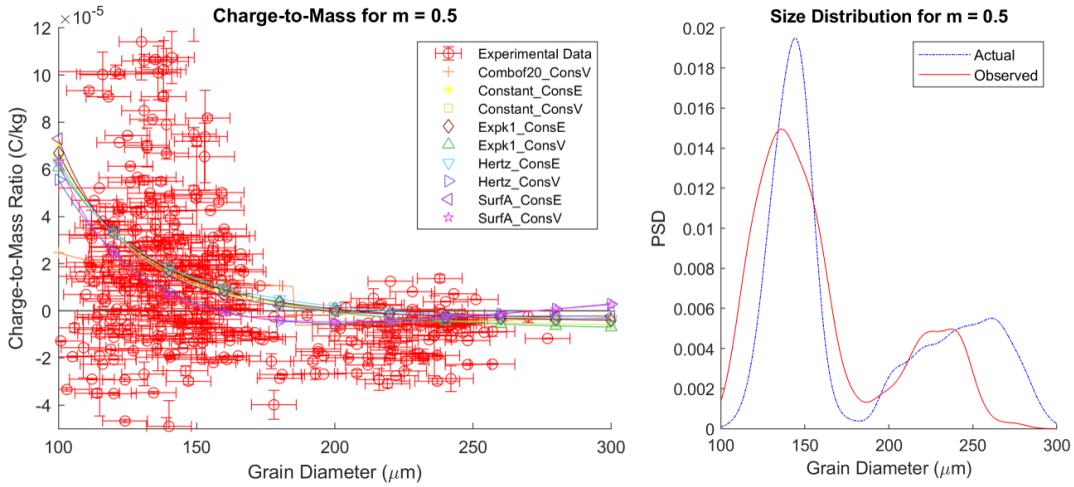

Figure 5.6: Results for mixtures composed of 1:2 small to large grains, by mass.

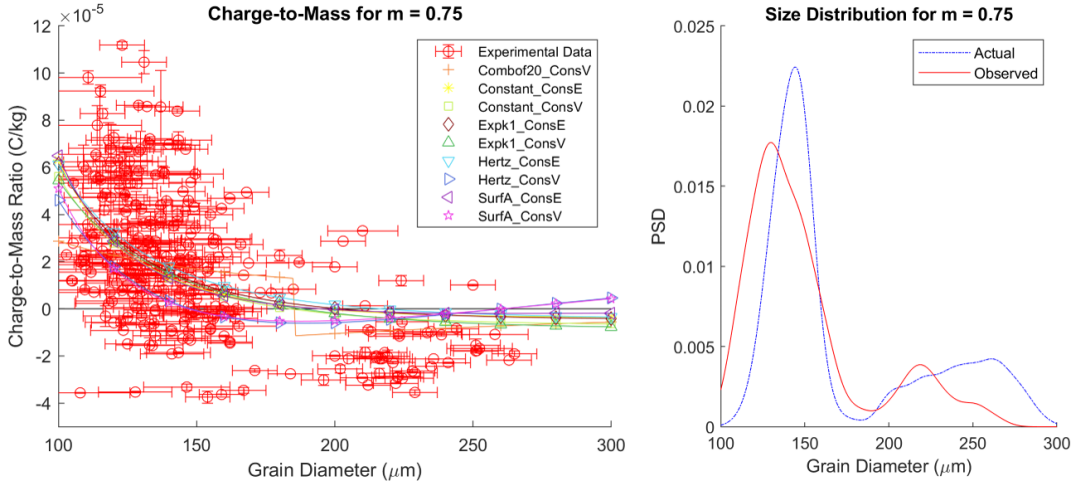

Figure 5.7: Results for mixtures composed of 3:4 small to large grains, by mass.

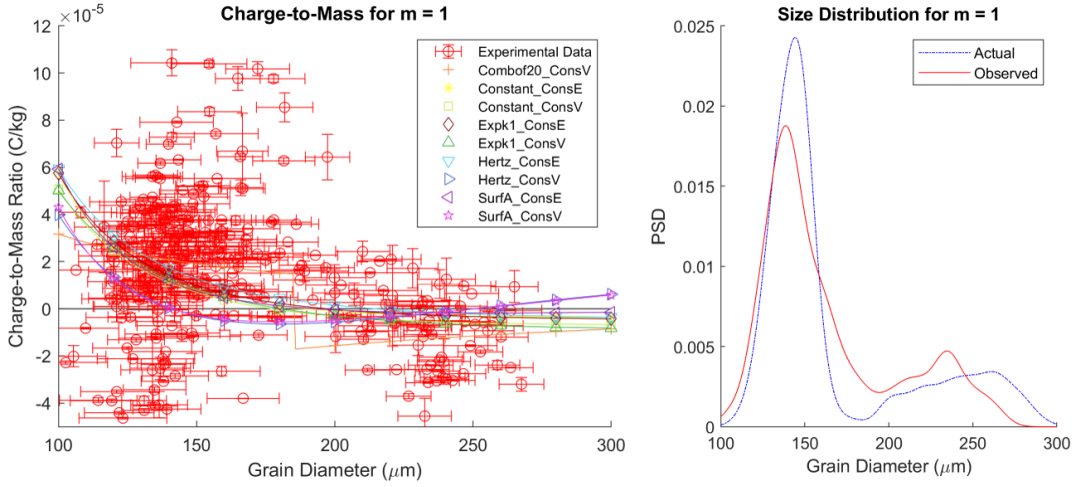

Figure 5.8: Results for mixtures composed of 1:1 small to large grains, by mass.

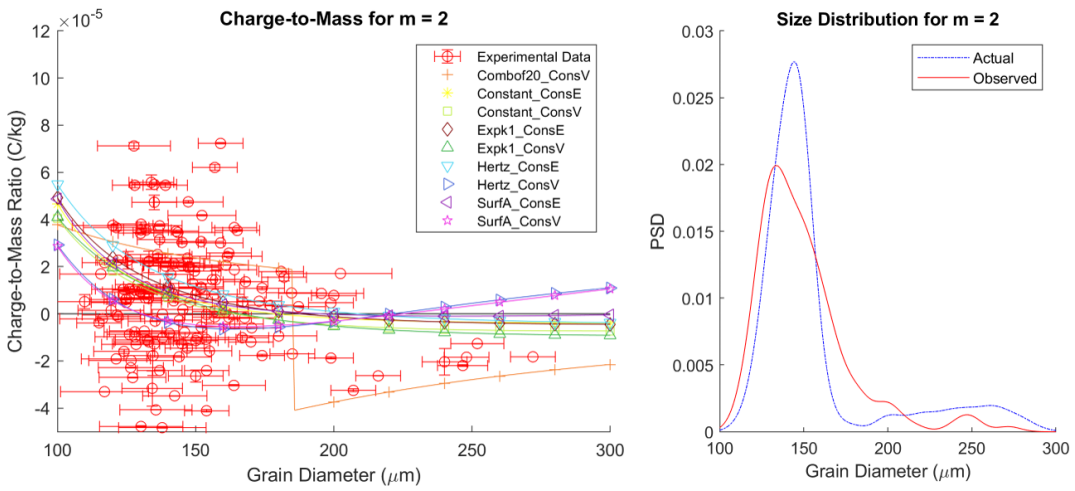

Figure 5.9: Results for mixtures composed of 2:1 small to large grains, by mass.

In Chapter 3, we predicted a reversal of the traditionally observed polarity, such that small grains would, on average, acquire a more positive charge, while large grains would acquire a negative charge [45]. This trend is supported by our results. There are a number of possible explanations for this effect. For one, the charging mechanism and environment are markedly different from that utilized in prior experiments. Other experiments frequently charge grains by fluidization a bed of grains with air or another gas [13, 21, 30, 34, 36]. In many cases, the results of these experiments have been examined through the lens of a collision model built on the same foundations as ours. As previously noted, conducting our experiment entirely in vacuum reduces the influence of recruited ions [29] and adsorbed water, which may be responsible for the prior observed polarity.

Additionally, we suspect that the collision rates assumed in prior models are poor representations of prior experimental methods. When the grains are fluidized from below, collisions primarily occur when grains launched by the flowing gas reimpact the bed. In addition to the significant rolling contacts that occur as the

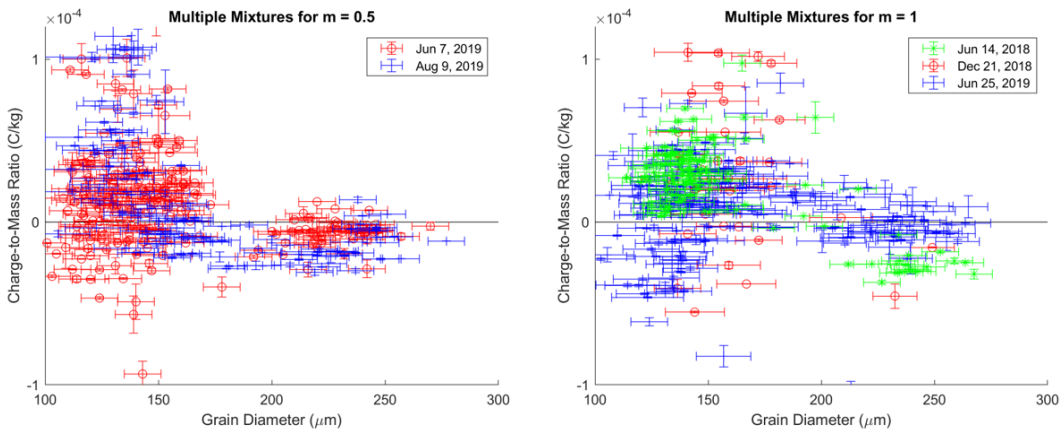

Figure 5.10: Data collected for the same mixtures on different days. All experiments shown high variance in charge magnitude and polarity, but approximately the same mean.

grains settle, there is likely to be a significant segregation of launched grains by size, with small grains launching more frequently and more energetically, which may skew the results. In some cases, these experiments also do not insulate the walls with the same material as the grains to prevent grain-to-wall charge transfer, allowing some of the more energetic grains to transfer charge in ways not accounted for by the collision model.

Each mixture presented in Figures 5.3 through 5.9 includes data taken from multiple videos of each of multiple separately-prepared mixtures. We display these identical mixtures, charged and measured in separate vacuum pumpdown events, on the same plot because we have observed that the charge magnitude and polarity crossover point are consistent in our experiments for mixtures with the same mass ratio. All mixtures are prepared in a consistent manner, but it is prudent to verify that each mixture still produces consistent results. In Figure 5.10 we can see the measured grain charge distributions for individual pumpdowns of select mixtures.

5.3 Model Fits

Each of the models described above assumes that the surface of each grain carries some finite initial density σ_0 of mobile charge carriers. Recall that the charge distribution function derived in Chapter 3 is directly proportional to this initial density. We have found the best fit of each model to the experimental data by varying this parameter. The charge carrier density σ_0 should be the same for all mixtures, so this parameter was found with a least-mean-square fit of the corresponding model predictions to all the data, weighted so that each mass ratio is weighted equally. The goodness of this fit is then measured using the R^2 value, which measures the ability of the model to account for the variance in the charge-to-mass ratio with diameter and is calculated as:

$$R^2 = 1 - \frac{SSE}{SST} \tag{5.1}$$

where SSE is the sum of squares of the residuals between the predicted and measured values, and SST is the sum of squares of the measured values about their overall mean. The results are shown in Figure 5.11. Note that the most accurate fits occur when $\sigma_0 < 0$; that is, the transferred charge species is a positively-charged species, rather than electrons. This has been observed in other experiments, leading some to suggest that the transferred charge species may in fact be OH^- ions or other ions recruited from the atmosphere [29]. The lack of an appreciable ambient atmosphere in our experiment rules out that possibility, but we cannot definitively

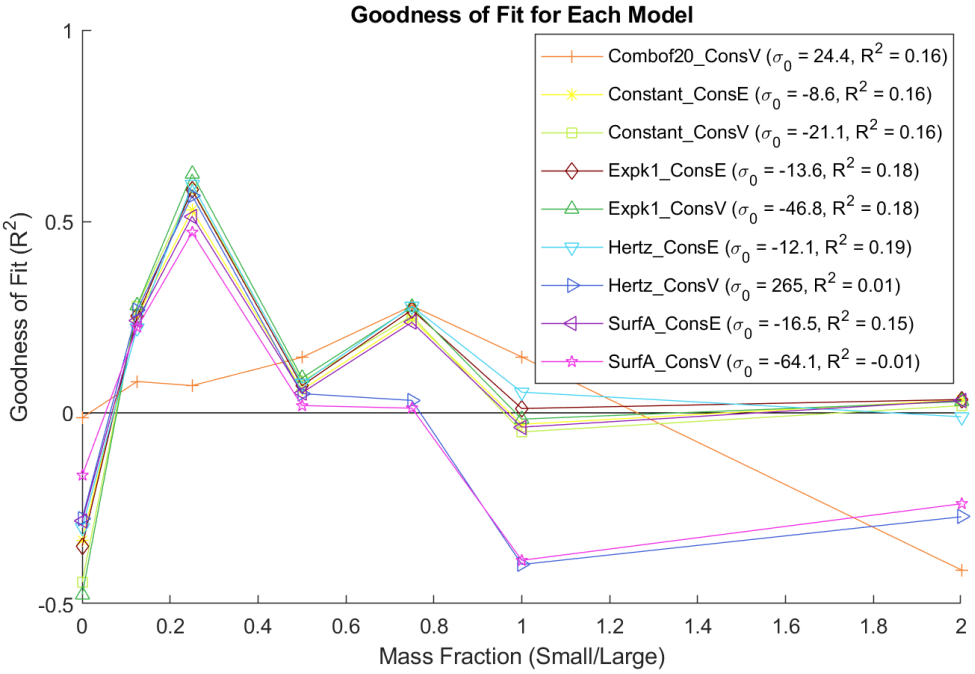

Figure 5.11: Goodness of fit over all data for the overall best-fit value of σ_0. Some experimental runs exhibited higher variance than others, resulting in poor fit confidence, but some fits are clearly better than others. Many indicate a negative charge carrier density, suggesting a positive species given our previous assumption of a negatively charged carrier.

say that there is no adsorbed water, as substantial bake-out is typically required to eliminate all water.

On first inspection of the goodness of fit curves, we note that many of the models follow the same patterns, fitting the data nearly equally well at all mass fractions. Unfortunately, we believe this to be a problem inherent to the high variance in the data itself, as has been observed in other experiments [13, 37, 38, 53]. R^2 essentially measures how well the fit explains the variance in the data compared to simply taking the mean of the data. However, when the variance is already so high and the mean of both the data and the fit are comparatively very small (as we expect net charge to be approximately zero), there is a risk of both the sum of

squares of the residuals and the total sum of squares being very large, in which case even reasonable models end up with R^2 values near or even below zero.

While many of the models demonstrated promising results, we can draw some conclusions from those that did not. For the Hertz_ConsV and SurfA_ConsV models, and to a lesser extent the combination model as well, we see that as the mass ratio increased, these models displayed increasingly poor performance. Following the curves of the constant-velocity Hertz and total surface area models, we can see that these models have zeroes at points that shift dramatically with changing mass ratio. For many mass ratios, these zeroes move near the centers of the size distribution peaks, suggesting a reversal occurring near that size fraction's mean diameter. This is not a trend that we see in the data, and the other models examined have polarity crossover points consistently nearer the midpoint between the two sizes.

The Combo models appear to fail for other reasons. This model has a discontinuity at the designated point separating large and small grains; this is to be expected, as the magnitude of charge transfer jumps dramatically for grains on either side of that point. While this model was, by design, able to consistently predict a polarity reversal between the two sizes, there is a great deal of inconsistency between this model and the magnitude of the charge segregation observed in the mixtures. Therefore, even if a material difference is present and does affect the charge distribution, we suspect that the effect of size differences still occurs to a pronounced degree, even dominating over the material differences.

Each of these least-accurate mixtures assumed a constant relative velocity for grains moving through the mixture during charging. Among the remaining models,

there is little difference in fit quality between models based on conservation of speed or energy. This is likely because, of all models presented, only the "Hertz" model uses a collision area dependent on the impact energy. In an equal-energy model, the large grains move slower than the small grains, but both still move against the same background of target grains. The collision rates against each species are different, but only in the Hertz model is the quantity of transferred charge in a single collision also affected by the equal-energy assumption.

Of all the models explored here, the model with the highest average fitness was the Hertz model [45], with the ConsE assumption. Many other models with the same energy assumption had similar fitness, and each of them required a negative density of charge carriers. Because our model assumes a negative charge carrier species, this is equivalent to the conclusion that the charge carriers are positively charged, with surface densities on the order of 8-47 charges per μm^2. Within this range, the lower values are based on the equal-energy models, with the higher values arising from the equal-speed models. This reveals that, when small grains have greater mobility than larger grains, the segregation of charge throughout the mixture becomes more pronounced. These results may also suggest that the collision energy plays a role in determining the quantity of charge transfer in a single collision, an effect captured by the Hertz model but not by the others presented here.

We note that, while the models presented here may not accurately capture the charging behavior on their own, these results demonstrate a method for assessing the viability of any arbitrary form of the collisional charge transfer. By using our model framework to generate a predicted charge distribution based on a transfer

mechanism, one can directly compare properties of the distribution to that of experimental results. For example, we noted that some transfer mechanisms yielded predicted charge distributions with two zeros, or with a single zero that shifted significantly with mixture mass ratio. As these behaviors were not observed in the experimental data, we are able to more confidently dismiss those proposed charge transfer mechanisms. We believe that more detailed analysis of the relationship between transferred charge per collision and the sizes and collision rates of the grains involved can yield quantitative measures for the validity of these models, which should dramatically improve the ability to identify the most likely candidates.

5.4 Conclusions

Using the experimental apparatus we developed, we measured how charge is distributed in mixtures composed of grains with two primary sizes. Despite the high variance in charge that naturally arises from the stochastic process of charging, which has impeded others' prior attempts to obtain such distributions, we are able to draw some conclusions about the charging process. We noted that the results of our experiments suggest that a positive charge species is likely to be responsbile for the observed charging, and we have presented a framework for determining the likelihood that a particular charge transfer mechanism is driving the charge transfer by comparing predictions of our model with the experimental results. This procedure can be followed to identify likely candidates based solely on the statistical properties of the predicted charge distribution.

Chapter 6: Conclusions and Next Steps

6.1 Contributions

This work has explored an elusive component of same-material granular dielectric tribocharging, a phenomenon which presents both challenges and opportunities for both terrestrial industries and space exploration. The small size of these grains, and their tendency to experience charge transfer or discharge when coming into contact with any other surface, make it difficult to measure individual grain charges in large quantities without manipulating the charge through the act of measurement itself. While it is clear that size-dependent charge segregation trends are occurring, the variance in the charge of a particular size fraction is significantly larger than the mean charge of that fraction. This makes it challenging to model or even observe the trends of the mean charge without a technique for accurately measuring the size and charge of individual grains. Our experiment provides the capability to do just that, in a compact mechanism that could be repeated in other laboratories with similar-sized vacuum chambers.

The establishment of an underlying framework for examining continuously distributed size distributions is a notable improvement itself. Many of the models that we explored through our predictive framework displayed different results for pseudo-

bidisperse continuous distributions, in which the continuous distribution consists of the sum of two normal distributions, than for the discretely bidisperse mixtures for which they were first designed. Our model can be used with any form for the charge transfer, relative grain speed, and even collision frequency, to predict how mean charge might be distributed in a mixture and identify better candidates to the transfer mechanism. This model, together with our robust experimental method for correlating charge with individual sizes, is a useful tool for exploring tribocharging in dielectric mixtures.

We have experimentally measured tribocharging in a broad range of zirconia-silica granular mixtures under ideal conditions. The highly spherical shape of the grains and our commitment to conducting all charging and measurement processes in vacuum creates conditions in which only material effects from grain-to-grain collisions are responsible for the tribocharging observed. Our data presents consistent observations that smaller grains charge positively and larger grains charge negatively under these conditions, a reversal from the results of many other experiments conducted in air and similar environments. This may be indicative of a confounding factor like ion recruitment or adsorbed humidity that has influenced the charging in those prior experiments. Our data can be used to identify where these effects may be occurring and guide the direction of theories for the underlying charging behavior in the absence of atmosphere, such as in airless environments like the Moon. A model such behavior could be used for *in-situ* resource utilization on the Moon or other dusty bodies for simple size and/or material beneficiation of the regolith.

Our predictive tribocharging model, when modified to assume equal kinetic

energy among grains and positive charge carriers, was among the most accurate models when compared to the charging data. We also identified other candidates for the charging mechanism that had reasonable accuracy as well. In particular, using a positive species with the exponential transfer model, though initially suggested to explain electron tunneling, gave a more reasonable fit compared to the other models presented. We also observed that in most cases, fewer charge carriers were necessary to account for the same degree of charging when assuming equally distributed kinetic energy than equal speed. Considering one of the most difficult questions in this area is how to reconcile the apparently low density of mobile charge carriers with the large grain charge magnitude resulting from tribocharging, this may suggest that collision models closer to the equal energy model are more accurate for our experient than those closer to constant velocity. Although assessing model fitness is difficult due to the high variance in charges, we believe that these results are promising and provide a path toward identifying more accurate models in the future.

6.2 Next Steps

With the development and verification of the results of our experiment, there are countless avenues for future investigation of granular mixtures using the same methods. We have primarily focused on pseudo-bidisperse mixtures of zirconia-silica, but the same experiment could be as easily conducted with other materials like glass or lunar regolith simulant, in any combination of sizes. For mixtures containing different materials or grains with irregular surface reflectivity, it may

be necessary to find solutions that increase the illumination on the grains, or that provide additional magnification.

We took many precautions to reduce the amount of water adsorbed onto the surface of our grains. The air in our laboratory was cycled through a dehumidifier, the grains were stored in sealed plastic bags with desicant packets to collect any residual moisture, and the chamber was kept under pressure when not in use to reduce adhesion of water to its interior. However, we do not have the means to verify conclusively through spectroscopic tests that water was not present on the grains during charging. It is likely that some water remained, though it is unclear whether this would be enough to have a significant impact on the charging process. To eliminate this effect, the grains should be baked at temperatures above boiling for a significant time (a day or longer) and promptly placed in the canister. Future iterations of this experiment may benefit from implementing these preprocessing procedures.

The experimental data we presented, combined with the predictions made by our model, are highly suggestive of a positive transferred charge species. Additional experimentation and analysis may provide more evidence for a particular mechanism behind this phenomenon. We recommend exploring complex, fully continuously distributed mixtures with broad size distributions, where the gap between the size fractions (and typically, therefore, the polarity) is not so large.

We also believe there is significant utility in exploring precisely how a proposed transfer species and mechanism relates to features of the predicted mean charge distribution generated by our model framework. For example, we observed that for

certain forms of the collision contact area, the point of zero polarity on the predicted mean charge changed significantly with mixture mass ratio, but for others, it did not. It is probable that the rate of change of the quantity of transferred charge relative to the rate of change of the size of the target grain, which is a property of the proposed mechanism alone, can be directly correlated to parameters like the grain size at the polarity crossover point. Developing an comprehensive understanding of this relationship would provide a method for quickly assessing the feasibility of any transfer mechanism. This, along with an in-depth study of other mixtures and materials, may provide the answers to the elusive nature of size-dependent charge segregation in granular media.

Bibliography

[1] T. Pahtz, H. Herrmann, and T. Shinbrot. Why do particle clouds generate electric charges? *Nature Physics*, 6:364–368, May 2010.

[2] J. Kok and N. Renno. Electrostatics in wind-blown sand. *Physical Review Letters*, 100, Jan 2008.

[3] X. Zheng, N. Huang, and Y. Zhou. Laboratory measurement of electrification of wind-blown sands and simulation of its effect on sand saltation movement. *Journal of Geophysical Research - Atmospheres*, 108, May 2003.

[4] J. Gilbert, S. Lane, R. Sparks, and T. Koyaguchi. Charge measurements on particle fallout from a volcanic plume. *Nature*, 349:598–600, Feb 1991.

[5] S. Liang, J. Zhang, and L. Fan. Electrostatic characteristics of hydrated lime powder during transport. *Industrial & Engineering Chemistry Research*, 35:2748–2755, Aug 1996.

[6] G. Hendrickson. Electrostatics and gas-phase fluidized bed polymerization reactor wall sheeting. *Chemical Engineering Science*, 61:1041–1064, Feb 2006.

[7] D. Saville, M. Al-Adel, and S. Sundaresan. The effect of static electrification on gas-solid flows in vertical risers. *Industrial & Engineering Chemistry Research*, 41:6224–6234, Dec 2002.

[8] P. Cartwright, S. Singh, A. G. Bailey, and L. J. Rose. Electrostatic charging characteristics of polyethylene powder during pneumatic conveying. *IEEE Transactions on Industry Applications*, 1985.

[9] M. Mazumder, S. Banerjee, and R. Ware. Characterization of triboelectric properties of powder paint. *IEEE Transactions on Industry Applications*, 30, Mar 1994.

[10] R. Mukherjee, V. Gupta, S. Naik, S. Sarkar, V. Sharma, P. Peri, and B. Chaudhuri. Effects of particle size on the triboelectrification phenomenon in pharmaceutical excipients: experiments and multi-scale modeling. *Asian Journal of Pharmaceutical Sciences*, 11:603–617, 2016.

[11] Daniel J. Lacks and Artem Levandovsky. Effect of particle size distribution on the polarity of triboelectric charging in granular insulator systems. *Journal of Electrostatics*, 65:107–112, Jul 2006.

[12] Daniel J. Lacks, Nathan Duff, and Sanat K. Kumar. Nonequilibrium accumulation of surface species and triboelectric charging in single component particulate systems. *Physical Review Letters*, 100(188305), May 2008.

[13] Keith M. Forward, Daniel J. Lacks, and R. Mohan Sankaran. Charge segregation depends on particle size in triboelectrically charged granular materials. *Physical Review Letters*, 102(028001), Jan 2009.

[14] J. Lowell and W. Truscott. Triboelectrification of identical insulators: I. an experimental investigation. *Journal of Physics D: Applied Physics*, 19:1273–1280, 1986.

[15] J. Lowell and W. Truscott. Triboelectrification of identical insulators: Ii. theory and further experiments. *Journal of Physics D: Applied Physics*, 19:1281–1298, 1986.

[16] S. Pence, V. Novotny, and A. Diaz. Effect of surface moisture on contact charge of polymers containing ions. *Langmuir*, 10:592–596, Feb 1994.

[17] J. A. Wiles, M. Fialkowski, M. R. Radowski, G. M. Whitesides, and B. A. Gryzbowski. Effects of surface modification and moisture on the rates of charge transfer between metals and organic materials. *Journal of Physical Chemistry B*, 108:20296–20302, Dec 2004.

[18] Y. Zhang, T. Pahtz, Y. Liu, X. Wang, R. Zhang, Y. Shen, R. Ji, and B. Cai. Electric field and humidity trigger contact electrification. *Physical Review X*, 5, Jan 2015.

[19] S. Pan and Z. Zhang. Fundamental theories and basic principles of triboelectric effect: a review. *Friction*, 1:2–17, Feb 2019.

[20] T. A. L. Burgo, T. R. D. Ducati, K. R. Francisco, K. J. Clinckspoor, F. Galembeck, and S. E. Galembeck. Triboelectricity: Macroscopic charge patterns formed by self-arraying ions on polymer surfaces. *Langmuir*, 28:7407–7416, 2012.

[21] Scott R. Waitukaitis, Victor Lee, James M. Pierson, Steven L. Forman, and Heinrich M. Jaeger. Size-dependent same-material tribocharging in insulating grains. *Physical Review Letters*, 112(218001), May 2014.

[22] N. Duff and D. J. Lacks. Particle dynamics simulations of triboelectric charging in granular insulator systems. *Journal of Electrostatics*, 66:51–57, 2008.

[23] J.F. Kok and D. J. Lacks. Electrification of granular systems of identical insulators. *Physical Review E*, 79, May 2009.

[24] T. Jackson, W. Farrell, and R. Killen. Discharging of roving objects in the lunar polar regions. *Journal of Spacecraft and Rockets*, 48, Jul 2011.

[25] S. Matsusaka, H. Maruyama, T. Matsuyama, and M. Ghadiri. Triboelectric charging of powders: A review. *Chemical Engineering Science*, 65:5781–5807, 2010.

[26] C. F. Gallo and W. L. Lama. Classical electrostatic description of the work function and ionization energy of insulators. *IEEE Transactions on Industry Applications*, 12:7–11, 1976.

[27] A. Diaz and R. Felix-Navarro. A semi-quantitative tribo-electric series for polymerica materials: the influence of chemical structure and properties. *Journal of Electrostatics*, 62:277–290, 2004.

[28] J. Henniker. Triboelectricity in polymers. *Nature*, 196, 1962.

[29] T. Shinbrot, T. Komatsu, and Q. Zhao. Spontaneous tribocharging of similar materials. *Europhysics Letters*, 83, Jul 2008.

[30] Huiliang Zhao, G. S. Peter Castle, Ion I. Inculet, and Adrian G. Bailey. Bipolar charging of poly-disperse polymer powders in fluidized beds. *IEEE Transactions on Industry Applications*, 39(3), May 2003.

[31] D. K. Davies. Charge generation on dielectric surfaces. *Journal of Physics D: Applied Physics*, 2(11):1533–1537, Nov 1969.

[32] J. Lowell and A. C. Rose-Innes. Contact electrification. *Advances in Physics*, 29(6):947–1023, 1980.

[33] T. Shinbrot. A look at charging mechanics. *Journal of Electrostatics*, 17:113–123, 1985.

[34] Huiliang Zhao, G. S. Peter Castle, and Ion I. Inculet. The measurement of bipolar charge in polydisperse powders using a vertical array of faraday pail sensors. *Journal of Electrostatics*, 55:261–278, Sep 2002.

[35] H. Watanabe, A. Samimi, Y. L. Ding, M. Ghadiri, and T. Matsuyama. Measurement of charge transfer due to single particle impact. *Particle and Particle Systems Characterization*, pages 133–137, 2006.

[36] K. M. Forward, D. J. Lacks, and R. M. Sankaran. Methodology for studying particle-particle tribo-electrification in granular materials. *Journal of Electrostatics*, 67:178–183, 2009.

[37] Keith M. Forward, Daniel J. Lacks, and R. Mohan Sankaran. Triboelectric charging of lunar regolith simulant. *Journal of Geophysical Research*, 114(A10109), Oct 2009.

[38] Keith M. Forward, Daniel J. Lacks, and R. Mohan Sankaran. Particle-size dependent bipolar charging of martian regolith simulant. *Geophysical Research Letters*, 36(L13201), Jul 2009.

[39] M. M. Apodaca, P. J. Wesson, K. J. M. Bishop, M. A. Ratner, and B. A. Grzybowski. Contact electrification between identical materials. *Angewandte Chemie - International Edition*, 49:946–949, 2010.

[40] M. Sow, R. Widenor, A. Kumar, S. W. Lee, D. J. Lacks, and R. M. Sankaran. Strain-induced reversal of charge transfer in contact electrification. *Angewandte Chemie - International Edition*, 51(11):2695–2697, 2012.

[41] S. Trigwell, J. G. Captain, E. E. Arens, J. W. Quinn, and C. I. Calle. The use of tribocharging in the electrostatic beneficiation of lunar simulant. *IEEE Transactions on Industry Applications*, 45(3), May 2009.

[42] S. Trigwell, J. E. Lane, J. G. Captain, K. H. Weis, J. W. Quinn, and F. Watanabe. Quantification of efficiency of beneficiation of lunar regolith. *Particulate Science and Technology*, 31(1):45–50, Jan 2013.

[43] S. Trigwell, J. G. Captain, K. H. Weis, J. W. Quinn, and E. Santiago-Maldonado. Evaluation of tribocharging electrostatic beneficiation of lunar simulant in lunar gravity. *Journal of Aerospace Engineering*, 26(1):37–42, Jan 2013.

[44] Scott R. Waitukaitis and Heinrich M. Jaeger. In situ granular charge measurement by free-fall videography. *Review of Scientific Instruments*, 84(025104), Feb 2013.

[45] D. Carter and C. Hartzell. Extension of discrete tribocharging models to continuous size distributions. *Physical Review E*, 95(012901), Jan 2017.

[46] T. Matsuyama and H. Yamamoto. Charge transfer between a polymer particle and a metal plate due to impact. *IEEE Transactions on Industry Applications*, 30:602–607, 1994.

[47] S. Matsusaka, M. Ghadiri, and H. Masuda. Electrification of an elastic sphere by repeated impacts on a metal plate. *Journal of Physics D: Applied Physics*, pages 2311–2319, 2000.

[48] D. Gugan. Inelastic collision and the hertz theory of impact. *American Journal of Physics*, 68(920), 2000.

[49] L. S. McCarty and G. M. Whitesides. Electrostatic charging due to separation of ions at interfaces: Contact electrification of ionic electrets. *Angewandte Chemie International Edition*, 47:2188–2207, Mar 2008.

[50] D. Carter and C. Hartzell. Experimental methodology for measuring in-vacuum granular tribocharging. *Review of Scientific Instruments*, 90(125105), Dec 2019.

[51] Keith M. Forward, Daniel J. Lacks, and R. Mohan Sankaran. Triboelectric charging of granular insulator mixtures due solely to particle-particle interactions. *Industrial & Engineering Chemical Research*, 48:2309–2314, 2009.

[52] John C. Crocker and David G. Grier. Methods of digital video microscopy for colloidal studies. *Journal of Colloid and Interface Science*, 179(0217):298–310, Sep 1995.

[53] J. Haeberle, A. Schella, M. Sperl, M. Schröter, and P. Born. Double origin of stochastic granular tribocharging. *Soft Matter*, 14:4987–4995, 2018.